

# System Performance Evaluation of Hybrid Beamforming with Shaped Beam Patterns for mm-Wave 5G Base Stations

Wenxu Chen





# System Performance Evaluation of Hybrid Beamforming with Shaped Beam Patterns for mm-Wave 5G Base Stations

Thesis report

by

Wenxu Chen

to obtain the degree of Master of Science  
at the Delft University of Technology  
to be defended publicly on June 29, 2023, at 9:00

Thesis committee: Prof. DSc. Olexander Yarovyi Professor, Chairman MS3 - TU Delft  
Dr. Remco Litjens Associate Professor NAS - TU Delft  
Senior Scientist TNO  
Dr. Yanki Aslan Assistant Professor MS3 - TU Delft  
Place: Faculty of Electrical Engineering, Mathematics and Computer Science,  
Delft University of Technology  
Project duration: November 2022 - June 2023  
Student number: 5403022

An electronic version of this thesis is available at <http://repository.tudelft.nl/>.



Copyright © Wenxu Chen, 2023  
All rights reserved.

# Acknowledgements

This master thesis has been a labor of love and an incredible journey, and I am deeply grateful to the many individuals and entities who have played a significant role in its completion. I would like to express my heartfelt appreciation to each of them.

To my esteemed daily supervisors, Dr. Yanki Aslan and Dr. Remco Litjens, I extend my deepest gratitude. Their unwavering support, guidance, and expertise have been invaluable throughout this research endeavor. Their ability to challenge my ideas, provide constructive feedback, and steer me in the right direction has been instrumental in shaping the outcome of this thesis. I am grateful for their patience, as they have consistently challenged me to think critically, pushed me beyond my comfort zone, and encouraged me to explore new avenues of research. Their ability to provide a balance of support and constructive critique has been invaluable, and I have grown both academically and personally under their guidance.

I am indebted to all members of the Microwave Sensing, Signals and Systems (MS3) group, whose dedication to teaching and scholarly pursuit has fostered an environment of academic excellence. Their intellectual insights, encouragement, and commitment to my development have played a pivotal role in my growth as a researcher. To merely name a few, thank you to Prof. DSc. Olexander Yarovy, for your exemplary leadership to bring together a diverse group of researchers and foster an environment that promotes interdisciplinary collaboration and innovation. Thank you to Ing. Fred van der Zwan and Ing. Antoon Frehe for making available the MS3 servers, without which I can't finish my simulations. Thank you to Esther de Klerk, your warm and approachable demeanor has created a welcoming atmosphere within the group.

To Maria Raftopoulou, thank you for engaging in my thesis, and providing me with useful information and feedback. I really enjoy our discussions.

Last but certainly not least, I would like to thank my family and friends for their unwavering support, encouragement, and belief in my abilities. Their love, understanding, and patience have sustained me during the challenges of this journey. I am grateful for their constant presence and the countless sacrifices they have made to enable me to pursue my academic aspirations.

Although it is impossible to acknowledge everyone individually, I want to express my sincere gratitude to all those who have played a part in shaping this thesis. Your support, encouragement, and belief in my abilities have been truly humbling and deeply appreciated.

Thank you all for being a part of this incredible journey and for contributing to the successful completion of this master thesis.

With sincere appreciation,

**Wenxu Chen**

# Abstract

Hybrid beamforming (HBF) architecture provides promising trade-offs between the system performance and computational/hardware complexity in practical implementations of millimeter wave (mm-Wave) massive multiple-input multiple-output (mMIMO) 5th generation (5G) mobile networks compared to its fully digital beamforming (DBF) counterpart. In this thesis, we investigate the future applicability of deploying hybrid beamforming architectures with subarray beam pattern shaping for mm-Wave 5G base stations in spatially heterogeneous user distributions and different propagation scenarios. We propose HBF structures with a cosecant-squared pattern and a flat-top pattern as well as their HBF and DBF benchmarks. In addition to the uniform user distribution, three non-uniform user distributions, i.e., the near-site distribution, the cell-center distribution, and the cell-edge distribution are proposed to represent the traffic flow and mobility of users due to festivals and holidays. We evaluate the performance in a novel 5G new radio (NR) system-level simulation (SLS) model. Numerical results show that the HBF architecture with a cosecant-squared subarray beam pattern is more robust against differences in spatially heterogeneous traffics than the flat-top HBF and benchmark HBF under the line-of-sight (LoS) propagation scenario. Under the non-line-of-sight (NLoS) propagation scenario, more deterministic environment information and radio channel modeling are required to improve the system performance of the shaped HBF beamforming technique.

**Keywords:** 5G, hybrid beamforming, massive MIMO, mm-Wave, system-level simulation

# Contents

|  |            |
|--|------------|
| <b>List of Abbreviations</b>                                   | <b>i</b>   |
| <b>List of Symbols</b>   | <b>iii</b> |
| <b>List of Figures</b>   | <b>iv</b>  |
| <b>List of Tables</b>  | <b>vi</b>  |
| <b>1 Introduction</b>  | <b>1</b>   |
| 1.1 5G Mobile Networks . . . . .                               | 1          |
| 1.2 Multibeam Antennas for 5G Base Stations . . . . .          | 2          |
| 1.3 Problem Definition . . . . .                               | 4          |
| 1.4 Research Objectives . . . . .                              | 5          |
| 1.5 Research Approach. . . . .                                 | 5          |
| 1.6 Related Work . . . . .                                     | 7          |
| 1.7 Novel Contributions . . . . .                              | 8          |
| 1.8 Thesis Outline. . . . .                                    | 9          |
| <b>2 System Model</b>  | <b>10</b>  |
| 2.1 Antenna Parameter Generation Block . . . . .               | 10         |
| 2.2 Radio Channel Generation Block . . . . .                   | 11         |
| 2.3 Beamforming Block . . . . .                                | 11         |
| 2.4 Link-to-System Mapping Block . . . . .                     | 13         |
| 2.5 Radio Resource Allocation Schemes . . . . .                | 16         |
| 2.6 Integration of Individual Blocks . . . . .                 | 18         |
| <b>3 Simulation Setting</b>                                    | <b>19</b>  |
| 3.1 Network Layout and User Distributions. . . . .             | 19         |
| 3.2 Beamforming Architectures. . . . .                         | 21         |
| 3.3 QuaDRiGa Parameter Setup . . . . .                         | 27         |
| <b>4 Results and Discussion</b>                                | <b>29</b>  |
| 4.1 Rank Strategy Selection . . . . .                          | 29         |
| 4.2 User Selection Scheme Configuration . . . . .              | 31         |
| 4.3 System Performance Evaluation . . . . .                    | 33         |
| 4.3.1 Line-of-Sight Scenario . . . . .                         | 33         |
| 4.3.2 Non-Line-of-Sight Scenario . . . . .                     | 41         |
| <b>5 Conclusion and Recommendations</b>                        | <b>44</b>  |
| <b>References</b>  | <b>47</b>  |
| <b>A Simulation Results for the Line-of-Sight Scenario</b>     | <b>51</b>  |
| <b>B Simulation Results for the Non-Line-of-Sight Scenario</b> | <b>54</b>  |

# List of Abbreviations

|               |   |                 |  |
|---------------|---|-----------------|--|
| <b>3GPP</b>   | 3rd generation partnership project                  | <b>IID</b>      | independent and identically distributed                    |
| <b>5G</b>     | 5th generation                                      | <b>ISD</b>      | intersite distance   |
| <b>ABF</b>    | analog beamforming                                  | <b>kHz</b>      | kilohertz  |
| <b>ADC</b>    | analog-to-digital converter                         | <b>L2SM</b>     | link-to-system mapping                                     |
| <b>AMC</b>    | adaptive modulation and coding                      | <b>LDPC</b>     | low density parity check                                   |
| <b>ARZF</b>   | adaptive regularized zero-forcing                   | <b>LLS</b>      | link-level simulation                                      |
| <b>AWGN</b>   | additive white Gaussian noise                       | <b>LNA</b>      | low-noise amplifier  |
| <b>BA</b>     | beam alignment                                      | <b>LoS</b>      | line-of-sight  |
| <b>BB</b>     | baseband  | <b>MBA</b>      | multibeam antenna  |
| <b>BLER</b>   | block error rate                                    | <b>MBPAA</b>    | multibeam phased array antenna                             |
| <b>BPSK</b>   | binary phase-shift keying                           | <b>Mbps</b>     | megabit per second   |
| <b>BS</b>     | base station  | <b>MCS</b>      | modulation and coding scheme                               |
| <b>CDF</b>    | cumulative distribution function                    | <b>MIB</b>      | mutual information per coded bit                           |
| <b>CESM</b>   | capacity effective SINR mapping                     | <b>MIESM</b>    | mutual information effective SINR mapping                  |
| <b>CQI</b>    | channel quality indicator                           | <b>MISO</b>     | multiple-input single-output                               |
| <b>CSI</b>    | channel state information                           | <b>mm-Wave</b>  | millimeter wave  |
| <b>D-MIMO</b> | distributed multiple-input multiple-output          | <b>mMIMO</b>    | massive multiple-input multiple-output                     |
| <b>DAC</b>    | digital-to-analog converter                         | <b>MMSE-IRC</b> | minimum mean square error-interference rejection combining |
| <b>DBF</b>    | digital beamforming                                 | <b>MR</b>       | maximum rate   |
| <b>DMBA</b>   | digital multibeam antenna                           | <b>MRT</b>      | maximum ratio transmission                                 |
| <b>DPC</b>    | dirty paper coding                                  | <b>MU-MIMO</b>  | multiuser multiple-input multiple-output                   |
| <b>DSP</b>    | digital signal processing                           | <b>NLoS</b>     | non-line-of-sight  |
| <b>EESM</b>   | exponential effective SINR mapping                  | <b>NR</b>       | new radio  |
| <b>F-OFDM</b> | filtered orthogonal frequency division multiplexing | <b>OMP</b>      | orthogonal matching pursuit                                |
| <b>FR2</b>    | frequency range 2                                   | <b>OSI</b>      | open systems interconnection                               |
| <b>Gbps</b>   | gigabit per second                                  | <b>OSPS</b>     | one-stream-per-subarray                                    |
| <b>GHz</b>    | gigahertz   | <b>PA</b>       | power amplifier  |
| <b>HARQ</b>   | hybrid automatic repeat request                     | <b>PF</b>       | proportional fairness                                      |
| <b>HBF</b>    | hybrid beamforming                                  | <b>PHY</b>      | physical layer   |
| <b>I-CSI</b>  | imperfect channel state information                 | <b>PMBA</b>     | passive multibeam antenna                                  |
|               |   | <b>PRB</b>      | physical resource block                                    |

**QAM** quadrature amplitude modulation  
**QPSK** quadrature phase-shift keying  
**QuaDRiGa** quasi deterministic radio channel generator  
**RE** resource element  
**RF** radio frequency  
**RIS** reconfigurable intelligent surface  
**RR** round robin  
**SCS** subcarrier spacing  
**SE** spectral efficiency  
**SINR** signal-to-interference-plus-noise ratio  
**SIW** substrate-integrated waveguide  
**SLS** system-level simulation  
**SM** spatial multiplexing  
**SNR** signal-to-noise ratio  
**SU-MIMO** single-user multiple-input multiple-output  
**SUS** semi-orthogonal user selection  
**SVD** singular value decomposition  
**TDD** time division duplex  
**TTI** transmission time interval  
**UE** user equipment  
**ULA** uniform linear array  
**UMa** urban macro  
**VP** vector perturbation  
**ZF** zero-forcing

# List of Symbols

|                         |   |                         |                                       |
|-------------------------|---|-------------------------|---------------------------------------|
| $(\cdot)^H$             | Hermitian conjugate operator                            | $\text{bdiag}\{\cdot\}$ | block diagonal matrix                 |
| $(\cdot)^{-1}$          | inverse operator  | $\text{diag}\{\cdot\}$  | diagonal matrix                       |
| $\alpha$                | normalization matrix of the channel<br>fullband average | $\theta$                | elevation angle                       |
| $\beta$                 | power constraint matrix of the pre-<br>coder            | $\tilde{\mathbf{S}}$    | reduced channel singular value matrix |
| $\zeta$                 | normalization matrix of the detector                    | $\tilde{\mathbf{U}}$    | reduced channel left singular matrix  |
| $\mathbf{G}$            | detection matrix  | $\tilde{\mathbf{V}}$    | reduced channel right singular matrix |
| $\mathbf{g}$            | detection vector  | $B$                     | bandwidth                             |
| $\mathbf{H}$            | channel matrix  | $B(\cdot)$              | block error rate measure function     |
| $\mathbf{I}$            | identity matrix   | $F$                     | noise figure                          |
| $\mathbf{S}$            | channel singular value matrix                           | $I(\cdot)$              | information measure function          |
| $\mathbf{U}$            | channel left singular matrix                            | $K$                     | number of users                       |
| $\mathbf{V}$            | channel right singular matrix                           | $k_B$                   | Boltzmann constant                    |
| $\mathbf{v}$            | channel right singular vector                           | $L$                     | number of layers                      |
| $\mathbf{W}$            | precoding matrix  | $m$                     | modulation order                      |
| $\mathbf{w}$            | precoding vector  | $N$                     | number of physical resource blocks    |
| $\delta$                | configuration parameter of the user<br>group selection  | $N_R$                   | number of receive antennas            |
| $\gamma$                | exponential smoothing factor                            | $N_T$                   | number of transmit antennas           |
| $\hat{R}$               | experienced instantaneous bit rate                      | $P$                     | proportional fairness ratio           |
| $\lambda$               | system noise-to-signal ratio                            | $P_{ns}$                | noise power                           |
| $\mathcal{X}$           | user group set  | $P_{tx}$                | transmitted power                     |
| $\overline{\mathbf{H}}$ | fullband-averaged channel matrix                        | $R$                     | average throughput                    |
| $\phi$                  | azimuth angle   | $r$                     | upcoming instantaneous bit rate       |
|                         |   | $t$                     | time snapshot                         |
|                         |   | $T_0$                   | noise temperature                     |

# List of Figures

|      |   |    |
|------|---|----|
| 1.1  | An example of the MU-MIMO precoding usage (reproduced from [3]) . . . . .   | 2  |
| 1.2  | Beamforming architectures in mm-Wave mMIMO systems [9] . . . . .  | 3  |
| 1.3  | Synthesis of a cosecant-squared beam pattern using the technique proposed in [13] . . . . .                                       | 4  |
| 2.1  | Schematic of the Antenna Parameter Generation block . . . . .   | 10 |
| 2.2  | Schematic of the Radio Channel Generation block . . . . .   | 11 |
| 2.3  | Schematic of the Beamforming block . . . . .  | 13 |
| 2.4  | BLER fitting curves for various MCS values corresponding to the channel quality indicators (CQIs) in Table 7.2.3-2 [39] . . . . . | 14 |
| 2.5  | Mutual information curves for different modulation schemes . . . . .  | 15 |
| 2.6  | Schematic of the Link-to-System Mapping block . . . . .   | 15 |
| 2.7  | Schematic of the 5G NR SLS model . . . . .  | 18 |
| 3.1  | Layout of a three-sectorized site . . . . .   | 19 |
| 3.2  | Uniform user distribution . . . . .   | 20 |
| 3.3  | Percentage of uniformly distributed users as a function of the antenna downtilt angle . . . . .                                   | 20 |
| 3.4  | Three non-uniform user distributions . . . . .  | 21 |
| 3.5  | Array antenna topology of benchmark DBF . . . . .   | 22 |
| 3.6  | Structure of the slot antenna element . . . . .   | 22 |
| 3.7  | 2D pattern of the slot antenna element at $\phi = 0^\circ$ cut . . . . .  | 23 |
| 3.8  | 3D pattern of the slot antenna element . . . . .  | 23 |
| 3.9  | Array antenna topology of HBF structures . . . . .  | 24 |
| 3.10 | Synthesis of proposed subarray beam patterns . . . . .  | 24 |
| 3.11 | 3D subarray antenna pattern of HBF with cosecant-squared shaping . . . . .  | 25 |
| 3.12 | 3D subarray antenna pattern of HBF with flat-top shaping . . . . .  | 25 |
| 3.13 | 2D subarray antenna pattern of benchmark HBF at $\phi = 0^\circ$ cut . . . . .  | 26 |
| 3.14 | 3D subarray antenna pattern of benchmark HBF . . . . .  | 26 |
| 3.15 | 2D subarray antenna pattern of different HBF structures at $\phi = 0^\circ$ cut . . . . .   | 26 |
| 3.16 | A 5G physical resource block (PRB) block and a resource element (RE) with 60 kHz subcarrier spacing . . . . .                     | 27 |
| 4.1  | Comparison of different fixed-rank strategies at the user level . . . . .   | 30 |
| 4.2  | Comparison of different fixed-rank strategies at the system level . . . . .   | 30 |
| 4.3  | Average user throughput versus the threshold $\delta$ . . . . .   | 32 |
| 4.4  | System throughput versus the threshold $\delta$ . . . . .   | 32 |
| 4.5  | CDF curves for different beamforming architectures with uniformly distributed 10 UEs under the LoS scenario . . . . .             | 34 |
| 4.6  | Comparison of shaped HBF structures and benchmarks with uniformly distributed 10 UEs under the LoS scenario . . . . .             | 35 |
| 4.7  | CDF curves for different beamforming architectures with non-uniformly distributed 10 UEs under the LoS scenario . . . . .         | 36 |

|      |   |    |
|------|---|----|
| 4.8  | Comparison of shaped HBF structures and benchmarks with non-uniformly distributed 10 UEs under the LoS scenario . . . . .                               | 37 |
| 4.9  | Comparison of shaped HBF structures and the benchmark HBF with mixed uniform and near-site user distributions under the LoS scenario (10 UEs) . . . . . | 38 |
| 4.10 | Comparison of shaped HBF structures and the benchmark HBF with mixed uniform and near-site user distributions under the LoS scenario (20 UEs) . . . . . | 39 |
| 4.11 | Comparison of shaped HBF structures and benchmarks with uniformly and non-uniformly distributed 20 UEs under the LoS scenario . . . . .                 | 40 |
| 4.12 | CDF curves for different beamforming architectures with uniformly and non-uniformly distributed 10 UEs under the NLoS scenario . . . . .                | 42 |
| 4.13 | Comparison of shaped HBF structures and benchmarks with uniformly and non-uniformly distributed 10 UEs under the NLoS scenario . . . . .                | 43 |
| A.1  | CDF curves for different beamforming architectures with uniformly and non-uniformly distributed 20 UEs under the LoS scenario . . . . .                 | 53 |

# List of Tables

|     |  |    |
|-----|--|----|
| 3.1 | An example of the base station parameter setup in QuaDRiGa with the benchmark DBF antenna model . . . . .  | 28 |
| 3.2 | UE parameter setup in QuaDRiGa . . . . .   | 28 |
| 3.3 | Network parameter setup in QuaDRiGa . . . . .  | 28 |
| 4.1 | Simulation parameters for the rank strategy selection . . . . .  | 29 |
| 4.2 | Simulation parameters for the user selection scheme optimization . . . . .   | 31 |
| 4.3 | Simulation parameters for the system performance evaluation . . . . .  | 33 |
| A.1 | 10th percentile CDF values for different beamforming architectures with uniformly and non-uniformly distributed 10 UEs under the LoS scenario . . . . .  | 51 |
| A.2 | 10th percentile CDF values for different beamforming architectures with uniformly and non-uniformly distributed 20 UEs under the LoS scenario . . . . .  | 52 |
| B.1 | 10th percentile CDF values for different beamforming architectures with uniformly and non-uniformly distributed 10 UEs under the NLoS scenario . . . . . | 54 |

# 1

## Introduction

In this chapter, the background information of 5G mobile networks and multibeam antenna technologies is introduced in Section 1.1 and 1.2. Afterward, the research problems are defined in Section 1.3, followed by the objectives of the research as given in Section 1.4. Section 1.5 provides an overview of the system model and simulation tools used in the thesis. The assumptions and research boundaries are described there as well. Section 1.6 furnishes the readers with a state-of-the-art literature review on system modeling and performance simulation of all forms of hybrid beamforming architectures. The contributions of this research to the scientific communities are summarized in Section 1.7. Finally, the structure of the thesis is outlined in Section 1.8.

### 1.1. 5G Mobile Networks

With continuously expanding data traffic and device connections, a new generation of wireless communication emerges roughly every decade, resulting in fundamental and profound impacts on the daily lives and social activities of human beings [1]. We are now at the right time for the 5th generation (5G) mobile networks. In such communication systems, the massive multiple-input multiple-output (mMIMO) technology serves as the key enabling technology for 5G throughput and resilience enhancement, allowing antenna arrays to transmit multiple signal beams to the user equipment (UE). The mMIMO technology clearly distinguishes itself from conventional MIMO systems by utilizing a very large number of antenna elements (e.g., 128) that operate fully coherently and adaptively, offering more flexible beams. To properly construct signal beams, beamforming is performed in downlink and uplink communications, which involves an important signal processing procedure before transmitting (i.e., precoding) and receiving (i.e., detection/combining) data streams. This procedure focuses the transmission signal energy on smaller areas and allows for greater spectral efficiency (SE) with less transmit power [2]. An example of the precoding usage in multiuser MIMO (MU-MIMO) systems is visualized in Figure 1.1.

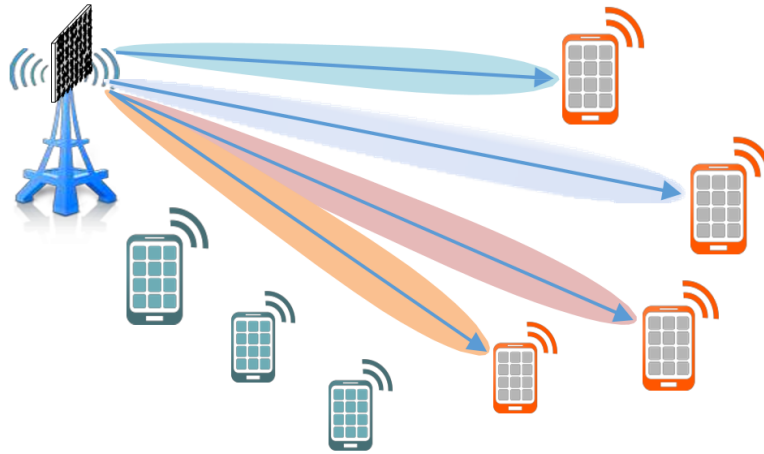


**Figure 1.1:** An example of the MU-MIMO precoding usage (reproduced from [3])

The high-demanding system performance requirements in the current 5G mobile network include a data transmission rate of a gigabit per second (Gbps), an extremely high traffic volume density, a latency time on the millisecond scale, super dense connections, and improved spectral, energy, and cost efficiencies [4]. In addition to smart beamforming, these high-level system properties will integrate advanced communication and network technologies incorporating adaptive modulation and coding (AMC) schemes such as low density parity check (LDPC) [5], hybrid automatic repeat request (HARQ) protocol [6], multiple access strategies, for example, filtered orthogonal frequency division multiplexing (F-OFDM) [7], and many others. The realization of these high-end technologies continuously challenges the physical infrastructure communities, among which, undoubtedly include the antenna system engineers. Driven by inevitably increasing demand for mobile data transmission speed and very limited available spectrum resources, the 5G wireless systems take a promising look at the millimeter wave (mm-Wave) frequency bands. It is well known that at high-frequency bands (i.e., frequency range 2 (FR2) at frequencies of 24 GHz and higher), the electromagnetic wave suffers from severe propagation losses and signal blockage, which substantially degrades the signal-to-interference-plus-noise ratio (SINR) and thus leads to lower bit rates [8]. To deal with this issue, the aforementioned mMIMO technology can be applied, which uses high-gain antenna arrays and directional beams to transmit the data streams to desired UEs. In such a technology, to overcome the shortcoming of antennas with a single-directive beam, multibeam antenna (MBA) technologies are proposed and will be introduced in the next section.

## 1.2. Multibeam Antennas for 5G Base Stations

The MBA antennas are capable of generating several concurrent but independent directive beams with a high gain value to cover a predefined angular range, providing a solution to overcome the drawbacks of antennas with a single-directive beam [1]. Hence, they provide a forward-looking solution to satisfy demanding system requirements for 5G wireless communications. According to [9], there are mainly three beamforming architectures in mm-Wave mMIMO systems: analog beamforming (ABF), digital beamforming (DBF), and hybrid beamforming (HBF). Their structures are shown in Figure 1.2. These architectures are applied to achieve MBA technologies. The MBAs are partitioned into passive MBAs (PMBAs), multibeam phased array antennas (MBPAAs), fully digital MBAs (DMBAs), fixed subarray DMBAs, and phased subarray DMBAs [1]. The PMBAs

are a class of MBAs that achieve the desired beamforming in the RF domain without using any active component [10]. They in general contain a finite number of well-isolated input ports. Each port is backed by a transceiver and controls a single narrow beam pointing at a predefined direction [1]. The MBPAAAs use the ABF approach and control signal beams in the analog domain. They can be subdivided into passive MBPAAAs and active MBPAAAs. The passive MBPAAAs possess a low-noise amplifier (LNA) and power amplifier (PA) for each beam; while for active MBPAAAs, every antenna element has individual LNA and PA.

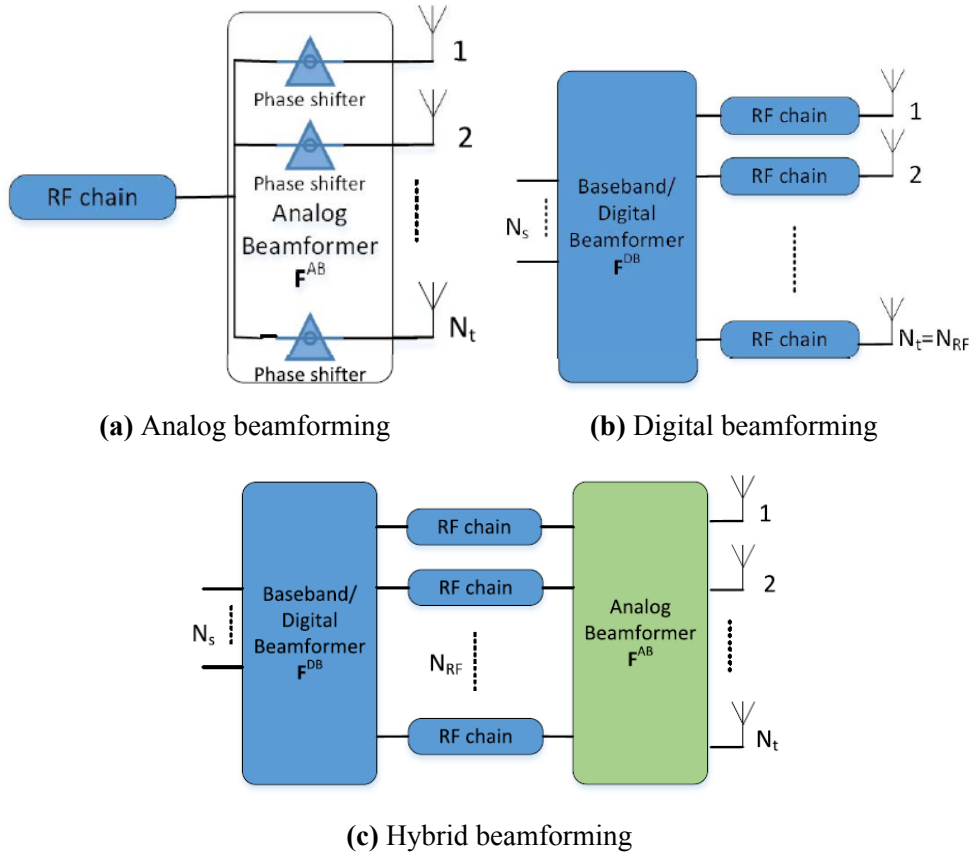


**Figure 1.2:** Beamforming architectures in mm-Wave mMIMO systems [9]

Full DMBAAs employ the DBF network and process beamforming in the baseband (BB) with high-precision digital signals. Each antenna element has a dedicated radio frequency (RF) chain as well as individual digital-to-analog converter (DAC) and analog-to-digital converter (ADC), thus the most flexibility in beam scanning can be achieved. However, [1] also states that at mm-Waves, to digitally synthesize beams simultaneously in parallel demands a considerable amount of computational resources. At mm-Waves, with low power amplifier efficiency and high energy consumption of high-speed digital signal processing (DSP) chips, active arrays in the order of  $8 \times 8$  or  $16 \times 16$  with a full DBF approach producing 3D adaptive multiple directional beams might not yet be economically competitive [11]. A promising and feasible alternative is to use arrays of vertical subarrays with shaped beam patterns (fixed subarray DMBAAs) and adapt multiple beams in the azimuth direction [12], [13]. This array structure employs the HBF method and looks at a compromise between low-power but less flexible ABF and power-hungry but fully flexible DBF solutions. The number of RF chains and DACs/ADCs connected to each subarray is

much reduced as compared to DBF. In the line-of-sight (LoS) condition with a cosecant-squared beam pattern, such a beamforming approach will help equalize the received power for users at different ranges and is beneficial for cell edge users [13], and resolve safety issues related to the vertical compliance distance since a single subarray antenna is formed in the vertical direction [14]. Moreover, compared to a large square array with DBF in azimuth and elevation, its hardware complexity, power consumption, and system cost are potentially much reduced. An example of a cosecant-squared beam pattern synthesis realized by a subarray comprising 12 radiating elements and two antenna feeding structures (i.e., center feed and end feed) as a function of the antenna downtilt angle is plotted in Figure 1.3. Herein, the wanted pattern is generated to ideally serve cell edge users by the main lobe of the antenna pattern, and the received power for users at different distances from the base station is equalized with the cosecant-squared pattern shaping.

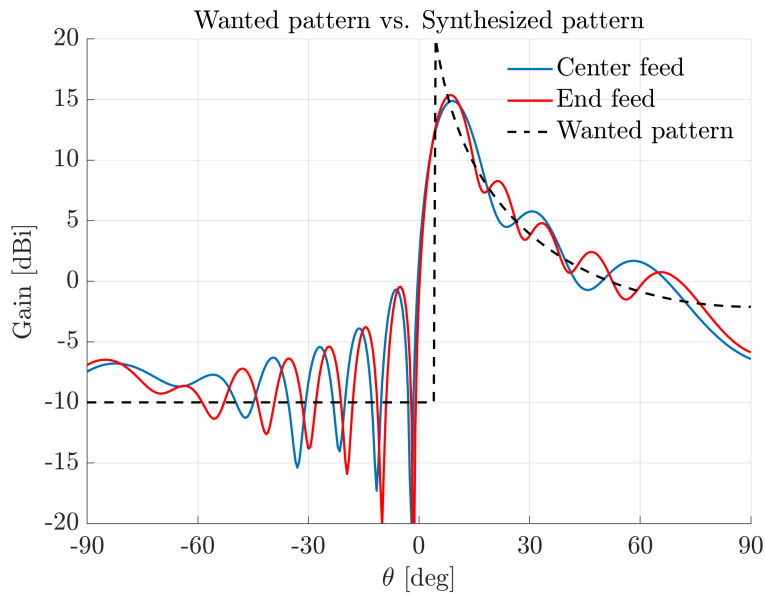


**Figure 1.3:** Synthesis of a cosecant-squared beam pattern using the technique proposed in [13]

### 1.3. Problem Definition

The existing works on the system performance simulation of hybrid beamforming architectures in mm-Wave 5G mobile networks (e.g., [15], [16]) used less realistic mm-Wave channel models (e.g., consider a single line-of-sight (LoS) or a single dominant non-line-of-sight (NLoS) path without multipath propagation), simplified system models (e.g., without incorporating the link-to-system mapping (L2SM) interface and advanced radio resource allocation schemes), or a simplified system performance evaluation metric (such as using sum spectral efficiency under the Shannon–Hartley theorem). Moreover, they generally assume only the uniform user distribution. The traffic flow and mobility of users due to festivals and holidays are ignored. Therefore, understanding and evaluating the applicability of such beamforming methods in close to real-life communication scenarios requires further and deeper system-level studies. This includes applying well-behaved beamforming algorithms, rigorous modeling of the antenna subarrays for a particular shaped beam pattern, defining signal propagation environment by using 3GPP standardized (and beyond) channel models and simulation tools (e.g., the QuaDRiGa radio channel generator [17]), and tailoring these to key system performance evaluation metric (e.g., system throughput including AMC schemes) with a smart selection of co-scheduled users.

Motivated by the aforementioned deficiencies in the present literature, two research questions are subsequently defined to center the thesis as follows:

#### Research Question 1

What are the trade-offs between the hybrid beamforming and fully digital beamforming architectures?

#### Research Question 2

What are the system performance variations of hybrid beamforming structures with shaped subarray beam patterns in spatially heterogeneous user distributions and different propagation scenarios?

## 1.4. Research Objectives

Based on the problem analysis, the objectives of the research are enumerated below:

- 1) Developing a novel 5G new radio (NR) system-level simulation (SLS) model at the 26 GHz frequency band that integrates the following parts:
  - Generation of the antenna parameters, including the number of elements, the elements spacing, the polarizations, and the excitation coefficients.
  - Generation of the radio channels that incorporate the antenna parameters, the UE movement profile, the network parameters, and the propagation scenarios.
  - Implementation of beamforming using advanced precoding and detection algorithms.
  - Realization of the link-to-system mapping interface, involving the SINR calculation, the effective SINR mapping, and the block error rate (BLER) prediction.
  - Application of intelligent radio resource scheduling and user group selection schemes.
- 2) Defining the system performance evaluation metric and demonstrating the trade-offs between HBF and DBF beamforming structures.
- 3) Evaluating the system performance variations of deploying HBF architectures with different subarray beam patterns (i.e., the cosecant-squared pattern and the flat-top pattern) in uniform/non-uniform user distributions and LoS/NLoS scenarios with multipath propagation.

## 1.5. Research Approach

This research uses a 5G NR system-level simulator (see Chapter 2) consisting of the Antenna Parameter Generation block, the Radio Channel Generation block, the Beamforming block, and the Link-to-System Mapping block. In addition, two smart radio resource allocation schemes (i.e., the proportional fairness (PF) scheduling and the semi-orthogonal user selection (SUS)) are also integrated into the model. A high-level overview of the SLS model is depicted in Figure 2.7. Most parts of the system model cover layer 1 (physical layer (PHY)) of the traditional open system interconnection (OSI) model, while the channel coding, BLER prediction, and radio resource scheduling are layer 2 (data link layer) functionalities. The SLS model covers nothing above layer 2. To reduce the computational complexity, the SINR metric is derived at the physical resource block (PRB) level and averaged over all PRBs of the carrier bandwidth (i.e., fullband-averaged),

which implies a flat channel assumption within individual PRBs. Hence, it ends up with a single choice of fullband modulation and coding scheme (MCS) per layer and per transmission time interval (TTI). The receiver noise is assumed independent and identically distributed (IID) and follows the Gaussian distribution.

In the Antenna Parameters Generation block, an iterative power synthesis technique is applied to taper the amplitude and phase distribution of each antenna element and reach the wanted pattern. The excitation coefficients are imported to CST Studio Suite [18], which then produces 3D subarray antenna patterns for further performance analysis. The antenna array of shaped HBF structures is a uniform linear array (ULA) that contains 32 subarrays in the azimuth direction. Each subarray is composed of 12 vertically stacked radiating elements and is dual-polarized (horizontal+vertical). To keep the array dimension consistent, the benchmark HBF antenna has the same size as shaped HBF structures, and the benchmark DBF antenna is of size  $12 \times 16$ . The benchmark HBF and DBF architectures are horizontally and vertically polarized as well.

QuaDRiGa, short for quasi deterministic radio channel generator, is an open-access software developed at Fraunhofer HHI for generating realistic radio channel impulse response for system-level simulation of mobile radio networks [17]. The QuaDRiGa channel model provides a reference implementation of the baseline 3rd generation partnership project (3GPP) channel models and implements modeling concepts and ideas that go beyond 3GPP (e.g., multifrequency simulation and spatial consistency) to support the more realistic channel simulations [19]. By nature, QuaDRiGa is a suitable tool for the theoretical justification and testing of 5G wireless mobile networks and is used in the radio channel generation block of the SLS model.

The works done in the thesis assume a single base station serving multiantenna UEs in one sector of a three-sectorized site. The channel state information (CSI), which describes how a signal propagates from the transmitter to the receiver (or vice versa), is assumed perfect for all downlink channels at the base station (BS). This assumption is reasonable for time division duplex (TDD) systems, as they allow the transmitter to exploit reciprocity between the downlink and uplink channels [3]. Zero-latency links (no CSI feedback delay) between the BS and UEs are assumed as well. Usually, the transmitter sends to a UE several layers in mMIMO systems, and the number of layers (rank) is less than the number of UE antennas. In the thesis, two fixed-layers (i.e., rank 2) that contain distinct signals (hence two data streams) are transmitted to each UE for spatial multiplexing (SM), and the rank adaptation problem (see e.g., [20]) is not considered for implementational simplicity. The base station power is equally shared among transmission layers and the power allocation problem is not addressed here. The focus of this research is on wireless system modeling and performance evaluation of various beamforming architectures. Therefore, the antenna designs are not explored in detail. More specifically, the mutual coupling effect among distinct (sub)arrays and within subarray antenna elements is ignored. The horizontally and vertically polarized antennas are modeled with identical patterns for a range of frequencies. This implies that the beam patterns of (sub)array antennas are not changed as a function of the operating frequency, polarization, or direction.

## 1.6. Related Work

Plenty of studies have addressed the performance simulation of hybrid beamforming for mm-Wave 5G communication systems, and some of the significant representatives are examined here in a critical manner. The performance of conventional fully-/sub-connected HBF systems is evaluated in several different forms [16], [21], [22]. In [16], a one-stream-per-subarray (OSPS) type of sub-connected HBF architecture is implemented. It consists of multiple subarrays and each connects to a single RF chain. In comparison to a fully connected architecture where each RF chain is connected to all BS antennas, the analog hardware complexity in terms of the number of phase shifters is much reduced. Furthermore, the realistic QuaDRiGa 3D channel simulator with 3GPP parameters for mm-Wave frequency bands (between 37 GHz and 40 GHz) is used. The system performance is evaluated based on per-user spectral efficiency in a multicarrier communication system. However, in this paper: (i) the antenna elements are designed with single-polarization (horizontal), and one data stream is transmitted to each UE. But in mobile networks, it is often desired to have two mutually orthogonal polarizations. In such a dual-polarization case, if one channel is weak, the other one might be strong, which allows it to effectively and simultaneously transmit multiple layers to a single UE. (ii) The SINR values are calculated and mapped to SE at the subcarrier level and the link-to-system mapping interface (see e.g., [23], [24]) is not implemented there. Hence, the BLER prediction conditioned on measurable physical parameters (e.g., SINR) for abstracting the link performance in the SLS model is not considered. (iii) The sets of users with sufficient angular separation are selected for the data communication. There is no scheduling algorithm (e.g., the proportional fairness scheduling [25], [26]) or user set selection scheme (e.g., the semi-orthogonal user selection [27], [28]) applied to the SLS model to effectively and efficiently assign radio resources to users in different time scales. (iv) The users are randomly distributed in a certain range from the base station and in each subrange of an azimuth range. The traffic flow and mobility of users in different locations of the hot spot are not modeled.

The studies done in [21], [22] compare the performance between fully-connected and sub-connected HBF architectures. To overcome the shortcomings of the literature outlined before, the authors in [21] use a more general and realistic mm-Wave channel model, more practical hardware impairments and hardware efficiency analysis, a joint evaluation of initial beam alignment (BA) and consecutive data communication, and low-complexity data transmit precoding. Numerical results show that the two architectures realized similar sum spectral efficiency, while the OSPS type is superior to the full-connected type in terms of hardware complexity and power efficiency. This paper again ignores/simplifies the implementations of antenna dual-polarization, multilayer transmission, L2SM interface, and a smart selection of co-scheduled users (a fixed number of users are simultaneously served instead). Moreover, the propagation channels between the BS and UEs work with multipath components instead of multicarrier components, which is not feasible to assign radio resources at the subband or fullband level. Similarly, [22] investigates the performance of two architectures under the same total transmission power. Differing from [21] where the conclusions are based on simulations, closed-form expressions of the sum rate for two architectures are derived. The results can accurately describe the system performance with different influencing factors including the number of users and signal-to-noise ratio (SNR). It is concluded that the fully-connected architecture can always achieve a better sum rate than the sub-connected architecture, and the difference is a constant when the SNR is high which is determined by the number of users. With low SNR, the performance difference can be neglected no matter what is the amount of users. However, this research assumes a multiple-input single-output (MISO) system and the UEs only have one antenna element. No detection algorithm is implemented and

the beamforming flexibility at the UE end is very limited. Moreover, the propagation channel models are approximated in closed forms by assuming the number of transmitting antennas grows to infinity and are not under realistic 3GPP standardization (such as the 3GPP-3D model [29] and the 3GPP-NR model [30]).

Besides fully-/sub-connected HBF approaches, the system modeling and simulation with a cosecant-squared beam pattern for received power equalization in 5G communication systems are studied in [15]. The novelty of this research lies in the adoption of the fixed subarray HBF approach with the cosecant-squared pattern shaping and performs beamforming in the azimuth direction. In comparison to the fully-/sub-connected HBF structures, the hardware complexity and cost are further reduced. There is no need of using RF phase shifters and the phase delays are controlled by physical phase elements within antenna subarrays. The simulation results prove that the cosecant-squared HBF with its all forms of azimuth beamforming outperforms the commonly used fully-connected HBF with orthogonal matching pursuit (OMP) algorithm for the 95 percent of total random user position realizations while providing a much-reduced implementation and processing complexity. However, in this research: (i) the receivers are equipped with a single isotropic antenna element, which is too idealistic. (ii) The modeling of radio channels is much simplified. It assumes that the propagation between the BS and UEs consists of a single LoS path or a single dominant NLoS path, which is far from realistic 3GPP-standardized channel models. (iii) The antenna dual-polarization, multicarrier system, multilayer transmission, and time evolution of the channels are ignored for simplicity. (iv) The system performance evaluation metric is oversimplified. The spectral efficiency is aggregated by randomly picking co-scheduled users from a uniform distribution within the sector on the ground, without incorporating AMC schemes, L2SM interface, BLER prediction, and intelligent radio resource scheduling schemes. (v) The users are uniformly distributed within the cell and non-uniform user distribution scenarios are not considered.

In conclusion, the state-of-the-art researches on performance simulation of hybrid beamforming architectures for mm-Wave 5G base stations use less realistic system models. Particularly, the modeling of radio channels is generally simplified, the system performance evaluation metric is idealistic, the L2SM interface is not implemented, and the radio resource allocation mechanism is too straightforward. Moreover, most of the studies do not consider heterogeneous user distributions in the presence of festivals and holidays. In the next section, the novel contributions of the thesis to the current literature are described.

## 1.7. Novel Contributions

To overcome the shortcomings in existing literature and understand the feasibility of deploying hybrid beamforming architectures with subarray beam pattern shaping, the system performance of using such a beamforming technique needs to be simulated in more realistic communication scenarios. The innovative research idea is to identify a suitable subarray beam pattern shape of the hybrid beamforming structure for mm-Wave 5G base stations. The main contributions of the thesis are summarized below:

- 1) ***Enhanced system-level simulation model.*** A novel 5G NR system-level simulation model is proposed in this research. Specifically, the SLS model integrates the following enhanced features:
  - The (sub)array antennas are modeled with two ports that can realize horizontal and vertical polarizations and enable multilayer transmission for spatial multiplexing.

- The QuaDRiGa radio channel generator is applied to the SLS model, which covers the baseline parts of the 3GPP channel models (e.g., the 3GPP-3D model and 3GPP-NR model) and implements modeling concepts that go beyond 3GPP (such as polarization and mobility of UEs) to support more realistic channel simulations.
  - The link-to-system mapping interface is implemented that captures the link-level performance of wireless systems conditioned on the effective SINR value, BLER prediction, and AMC schemes.
  - The proportional fairness scheduling algorithm that fairly serves users while maximizing the system capacity, and the semi-orthogonal user selection scheme are combined to smartly assign radio resources among users in different time slots.
- 2) ***Performance simulation in spatially heterogeneous user distributions.*** To model the traffic flow and mobility of users due to festivals and holidays, several spatially heterogeneous user distribution scenarios are proposed. In addition to uniform user distribution, three cases of non-uniform user distribution in different locations of the hot spot are generated. The performance of deploying diverse beamforming architectures is evaluated based on the proposed heterogeneous user distribution scenarios. A favorable user distribution case where shaped HBF structures significantly outperform the benchmark is found.

## 1.8. Thesis Outline

The rest of the thesis is organized as follows. The novel 5G NR SLS model is explained in Chapter 2. Chapter 3 introduces the simulation setting to configure radio channels. The results of applying the SLS model in various beamforming structures, user distributions, and propagation scenarios are presented and analyzed in Chapter 4. Finally, the conclusion of the thesis and several promising directions for future work are provided in Chapter 5.

# 2

## System Model

The 5G NR system-level simulation model is introduced in this chapter. The SLS model consists of four interrelated blocks, i.e., the Antenna Parameter Generation block, the Radio Channel Generation block, the Beamforming block, and the Link-to-System Mapping block. These blocks are explained in Section 2.1 to Section 2.4 respectively. In Section 2.5, the proportional fairness packet scheduling and semi-orthogonal user selection algorithms are illustrated. Lastly, the individual blocks and the two radio resource sharing schemes are integrated to generate the complete system model in Section 2.6.

### 2.1. Antenna Parameter Generation Block

The SLS model starts from the Antenna Parameter Generation block, as shown in Figure 2.1. The goal is to generate the antenna parameters of beamforming architectures under test in QuaDRiGa. To achieve this goal, user distribution scenarios should be obtained to determine where users are located and how they are distributed. Based on that, the 2D subarray antenna pattern of the HBF beamforming method can be created. The wanted pattern is synthesized using an in-house developed iterative power synthesis technique as proposed in [13]. As a result, the array factor is acquired and fed into CST Studio Suite to create a 3D subarray antenna pattern. The 3D pattern is then converted into QuaDRiGa antenna parameters for radio channel generation. For the DBF beamforming approach, the beam pattern synthesis process is not needed. The QuaDRiGa antenna parameters are generated directly from CST Studio Suite with a 3D array antenna pattern.

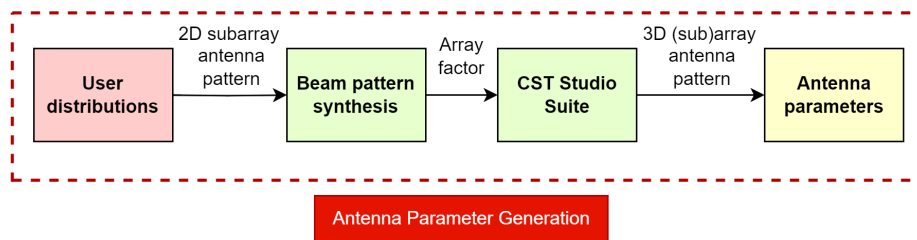


**Figure 2.1:** Schematic of the Antenna Parameter Generation block

## 2.2. Radio Channel Generation Block

The next is the Radio Channel Generation block, as visualized in Figure 2.2. To configure wireless communication channels, the antenna parameters, the User movement profile, the network parameters, and the propagation scenarios are required. Among them, the antenna parameters are provided by the previous block. These parameters are input to the QuaDRiGa channel generator for calculating time-evolving channel coefficients. The dimensions of the complex-valued channel matrix for a given UE are the number of receive antennas, the number of transmit antennas, the number of PRBs, and the number of time snapshots.

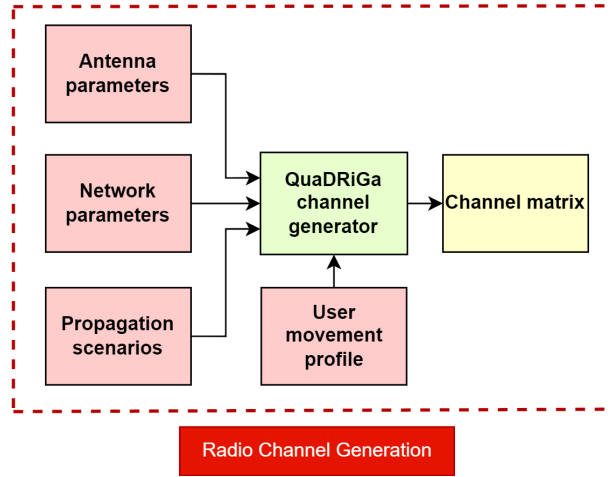


Figure 2.2: Schematic of the Radio Channel Generation block

## 2.3. Beamforming Block

Applying the channel matrix derived from the Radio Channel Generation block, beamforming can be subsequently performed as shown in Figure 2.3. To abstract the MIMO channel information, instead of the full matrix of the UE channel, vectors from its singular value decomposition (SVD) are used. Such an SVD decomposition of the full channel matrix is widely applied in many existing studies on wireless systems [3], [31], [32]. The mathematics behind the SVD application in MIMO communication systems is explained here. Considering a cellular network configured with  $K$  UEs and  $N_T$  transmit antennas. Each UE  $k$  is equipped with  $N_{R_k}$  antennas, and there are in total  $N_R = \sum_{k=1}^K N_{R_k}$  receive antennas. The channel matrix of UE  $k$  is first fullband-averaged in the form  $\bar{\mathbf{H}}_k = \alpha \cdot \frac{1}{N} \sum_{n=1}^N \mathbf{H}_{k,n}$  for each time snapshot  $t$ , where  $\alpha = \frac{\sum_{n=1}^N \|\mathbf{H}_{k,n}\|}{\|\sum_{n=1}^N \mathbf{H}_{k,n}\|}$  is the normalization matrix.  $\bar{\mathbf{H}}_k$  is in the dimension of  $N_{R_k} \times N_T$ , where the time index is omitted for simplicity of notation. According to [3], the SVD decomposition of fullband-averaged channel matrix can be written in the following form:

$$\bar{\mathbf{H}}_k = \mathbf{U}_k^H \mathbf{S}_k \mathbf{V}_k \quad (2.1)$$

herein,  $\mathbf{U}_k \in \mathbb{C}^{N_{R_k} \times N_{R_k}}$  is channel left singular matrix,  $\mathbf{S}_k = \text{diag}\{s_1, s_2, \dots, s_{N_{R_k}}\} \in \mathbb{R}^{N_{R_k} \times N_{R_k}}$  is a diagonal matrix that sorts channel singular values in descending order, and  $\mathbf{V}_k \in \mathbb{C}^{N_{R_k} \times N_T}$  is channel right singular matrix. The channel matrix is thereby decomposed into a number of independent eigenmodes [31]. These eigenmodes are mutually orthogonal to each other and are ordered with non-equal gains corresponding to their path losses. In [3], it is proposed to naturally

choose the first  $L_k$  ( $L_k \leq N_{R_k}$ ) vectors from  $\mathbf{V}_k$  that corresponds to  $L_k$  strongest layers in MIMO channels. After determining the number of transmission layers, the SVD components are reduced to  $\tilde{\mathbf{U}}_k \in \mathbb{C}^{L_k \times N_{R_k}}$ ,  $\tilde{\mathbf{S}}_k \in \mathbb{R}^{L_k \times L_k}$ , and  $\tilde{\mathbf{V}}_k \in \mathbb{C}^{L_k \times N_T}$ . Now, considering  $K$  UEs co-scheduled by  $L = \sum_{k=1}^K L_k$  data streams, the follow representation holds [3]:

$$\overline{\mathbf{H}} \approx \tilde{\mathbf{U}}^H \tilde{\mathbf{S}} \tilde{\mathbf{V}} \quad (2.2)$$

in Equation 2.2,  $\overline{\mathbf{H}} = \{\overline{\mathbf{H}}_1; \overline{\mathbf{H}}_2; \dots; \overline{\mathbf{H}}_K\} \in \mathbb{C}^{N_R \times N_T}$ ,  $\tilde{\mathbf{U}} = \text{bdiag}\{\tilde{\mathbf{U}}_1, \tilde{\mathbf{U}}_2, \dots, \tilde{\mathbf{U}}_K\} \in \mathbb{C}^{L \times N_R}$ ,  $\tilde{\mathbf{S}} = \text{bdiag}\{\tilde{\mathbf{S}}_1, \tilde{\mathbf{S}}_2, \dots, \tilde{\mathbf{S}}_K\} \in \mathbb{R}^{L \times L}$ , and  $\tilde{\mathbf{V}} = \{\tilde{\mathbf{V}}_1; \tilde{\mathbf{V}}_2; \dots; \tilde{\mathbf{V}}_K\} \in \mathbb{C}^{L \times N_T}$ , where  $\text{bdiag}\{\cdot\}$  denotes the block diagonal matrix. Note that this formulation is not strictly the SVD decomposition of full channel matrix  $\overline{\mathbf{H}}$ , but rather the concatenation of single UE partial SVD decomposition. The vectors  $\tilde{\mathbf{V}}_{i,l}$ ,  $\tilde{\mathbf{V}}_{j,l}$  ( $i \neq j$ ) corresponding to layers emitted to different UEs are generally not mutually orthogonal. Bobrov *et al.* in [3] stated that it is sufficient to use the reduced channel matrix  $\tilde{\mathbf{V}}$  for beamforming, which is much simpler than using the full channel matrix  $\overline{\mathbf{H}}$ .

After the SVD decomposition of the full channel matrix, beamforming is performed to obtain the fullband precoder and detector. At the transmitter end, the adaptive regularized zero-forcing (ARZF) precoding algorithm is chosen considering multiuser transmission, which outperforms conventional maximum ratio transmission (MRT) and zero-forcing (ZF) precoding algorithms [3], [33]. The analytic formula of an ARZF precoder  $\mathbf{W} \in \mathbb{C}^{N_T \times L}$  can be expressed as following:

$$\mathbf{W} = \beta \tilde{\mathbf{V}}^H (\tilde{\mathbf{V}} \tilde{\mathbf{V}}^H + \lambda \tilde{\mathbf{S}}^{-2})^{-1} \quad (2.3)$$

wherein  $\beta$  is the power constraint matrix. Since the power allocation problem is not considered here, the base station power is uniformly distributed over the transmission layers, which implies a vector normalization in the form  $\beta = \sqrt{\frac{P_{tx}}{L}} \left[ \frac{1}{\|\mathbf{w}_1\|} \dots \frac{1}{\|\mathbf{w}_L\|} \right]$ .  $(\cdot)^H$  is the Hermitian conjugate operator.  $\tilde{\mathbf{V}}$  and  $\tilde{\mathbf{S}}$  are the reduced SVD components of the full channel matrix, and  $\lambda \tilde{\mathbf{S}}^{-2}$  is the diagonal regularization matrix with  $\lambda = \frac{L P_{ns}}{P_{tx}}$  the system noise-to-signal ratio. In the scenario of single-user transmission, the MRT precoding algorithm [3], [33] will be applied to maximize the signal power.

At the receiver end, for each UE  $k$ , the minimum mean square error-interference rejection combining (MMSE-IRC) [34] detection algorithm is applied. A MMSE-IRC detector  $\mathbf{G}_k \in \mathbb{C}^{L_k \times N_{R_k}}$  realizes the following rule:

$$\mathbf{G}_k = \zeta (\overline{\mathbf{H}}_k \mathbf{W}_k)^H (\overline{\mathbf{H}}_k \mathbf{W} (\overline{\mathbf{H}}_k \mathbf{W})^H + \lambda \mathbf{I})^{-1} \quad (2.4)$$

in Equation 2.4, the normalization matrix  $\zeta = \left[ \frac{1}{\|\mathbf{g}_1\|} \dots \frac{1}{\|\mathbf{g}_{L_k}\|} \right]$ ,  $\lambda$  is the system noise-to-signal ratio, and  $\mathbf{I}$  is an identity matrix of dimension  $N_{R_k} \times N_{R_k}$ .

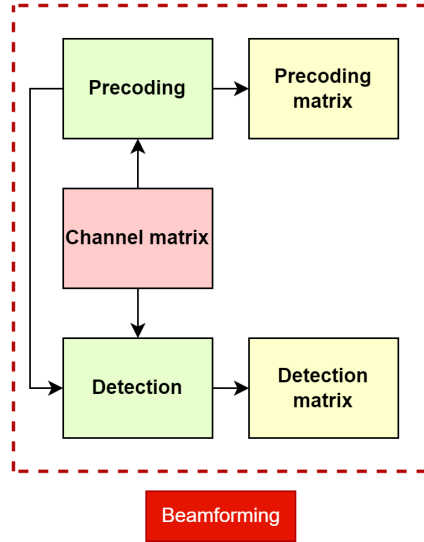


**Figure 2.3:** Schematic of the Beamforming block

## 2.4. Link-to-System Mapping Block

In multicarrier communication systems, usually, researchers divide the performance evaluation based on computer simulation into the link-level simulation (LLS) and system-level simulation (SLS) [23], [35], [36]. The main purpose of LLS simulation is to assess the performance of an individually isolated link in the physical layer (PHY) of wireless systems. The link performance features are typically dependent on channel modulation and coding schemes (MCSs), small/large-scale fading, and shadow fading, and are assessed by calculating the SINR value per subcarrier. Meanwhile, methods of the block error rate (BLER) prediction conditioned on measurable physical parameters (e.g., SINR) are required for modeling the link performance in SLS [24]. To achieve this, an interface that is known as link-to-system mapping (L2SM) is implemented, as plotted in Figure 2.6. The essence of the L2SM interface is to capture link-level performance based on SINR values versus BLER probabilities.

To compute SINR values, the channel matrix, precoding matrix, and detection matrix are required from previous blocks. The PRB-level noise power can be calculated via  $P_{ns} = Fk_B T_0 B$ , where  $F$  is the noise figure,  $k_B$  is the Boltzmann constant,  $T_0$  is the noise temperature, and  $B$  is the bandwidth of a PRB block. Together with fullband beamformers, the per-layer and per-PRB SINR function for UE  $k$  is defined as:

$$SINR_{l,n} = \frac{|g_l \mathbf{H}_{k,n} \mathbf{w}_l|^2}{\sum_{i \neq l}^L |g_l \mathbf{H}_{k,n} \mathbf{w}_i|^2 + P_{ns}} \quad (2.5)$$

note that the channel matrix used in the SINR calculation is not fullband-averaged.

Hanzaz *et al.* in [36] stated that the main challenge of the L2SM interface is the assessment of link-level performance conditioned on multicarrier and multilayer transmission. In such systems, the SINR measurements vary greatly with time and frequency due to the multipath fading effect. As a result, the instantaneous measure of channel quality will have multistate values. It is computationally intensive to assess the link performance based on multistate values at the subcarrier/PRB level. Therefore, the SINR measurements should be compressed into an effective value that counts for all transmit blocks of the fullband spectrum. This process is named effective

SINR mapping (ESM). The principle of ESM mapping is introduced here. Firstly, the per-layer effective SINR ratio can be derived in the following form [37]:

$$SINR_{l,eff} = I^{-1} \left( \frac{1}{N} \sum_{n=1}^N I(SINR_{l,n}) \right) \quad (2.6)$$

herein,  $I(\cdot)$  represents the “information measure” function of the SINR value for each layer and PRB, and  $I^{-1}(\cdot)$  is its inverse. The effective SINR is subsequently mapped to the corresponding BLER probability. To ensure accuracy, according to [37], the following approximation must be fulfilled for most of the channel realizations:

$$B(\{SINR_{l,n}\})_{MCS} \approx B_{AWGN}(SINR_{l,eff})_{MCS} \quad (2.7)$$

where  $B(\cdot)$  is the function that estimates BLER probabilities conditioned on instantaneous channel state (i.e., SINR) for various MCS schemes. The realization of such functions for 5G communications up to 256 quadrature amplitude modulation (QAM) is plotted in Figure 2.4 (reproduced based on [38]). In Equation 2.7, the left side computes actual BLER probabilities and the right side calculates predicted BLER probabilities in additive white Gaussian noise (AWGN) channels.

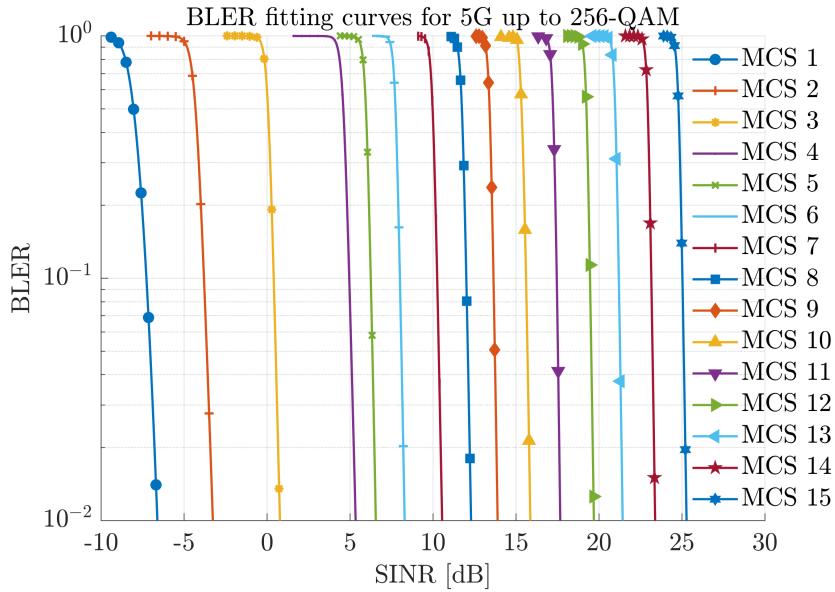


**Figure 2.4:** BLER fitting curves for various MCS values corresponding to the channel quality indicators (CQIs) in Table 7.2.3-2 [39]

Several ESM methods exist in the literature, such as capacity ESM (CESM), exponential ESM (EESM), and mutual information ESM (MIESM) [37]. Compared to other techniques, the MIESM method doesn't require fine optimization and calibration processes to compute the adjusting factor for each MCS and therefore is applied to the L2SM block. In MIESM mapping, the information is measured by a nonlinear function  $I_m(SINR_n)$  that subjects to the modulation order  $m$  [24].  $m = \{1, 2, 4, 6, 8\}$  corresponding to binary phase-shift keying (BPSK), quadrature phase-shift keying (QPSK), 16-QAM, 64-QAM, and 256-QAM respectively. It was shown in [24] that the mutual information per coded bit (MIB) function  $I_m(\cdot)$  can be numerically approximated and

stored for link performance prediction. Based on studies [23], [24], [40], the mutual information curves for different modulation schemes are plotted as shown in Figure 2.5.

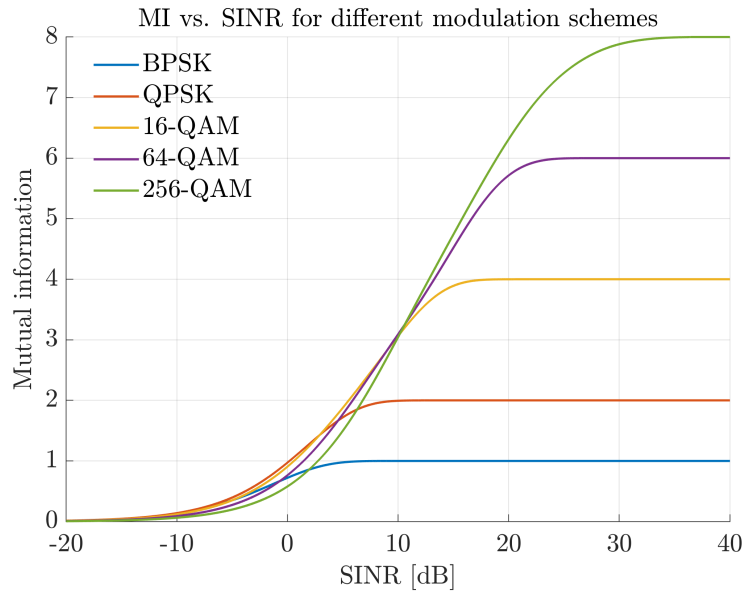


**Figure 2.5:** Mutual information curves for different modulation schemes

To sum up, in the L2SM block, the link-level SINR values are first calculated. Afterward, the SINRs are mapped to an effective SINR value using the MIESM mapping method assuming that the 256-QAM modulation scheme is applied. Then, together with the BLER curves, the actual MCS scheme can be determined such that the BLER probability doesn't exceed the threshold (i.e., 10% in this study). Finally, the bit rate of each transmission layer is obtained.

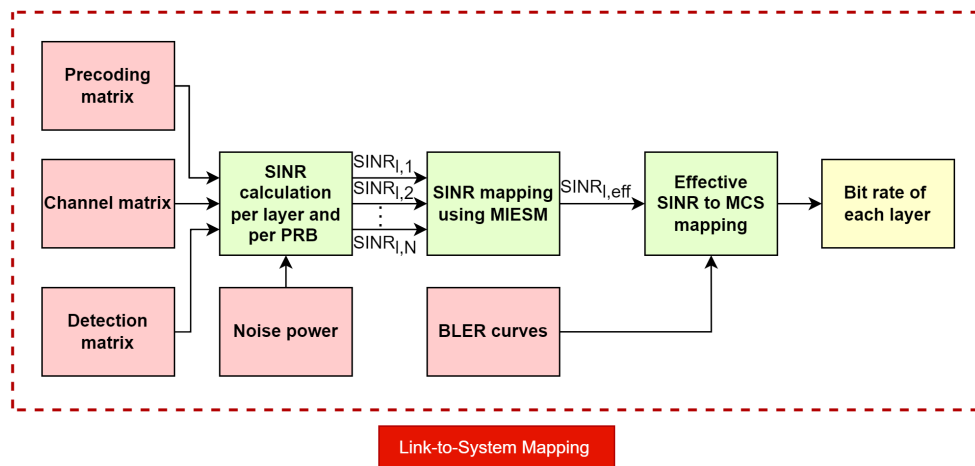


**Figure 2.6:** Schematic of the Link-to-System Mapping block

## 2.5. Radio Resource Allocation Schemes

To efficiently and effectively assign radio resources to users at different time scales, two advanced radio resource allocation mechanisms are applied to the SLS model. Namely, the proportional fairness (PF) scheduling [25], [26] and the semi-orthogonal user selection (SUS) [27], [28].

According to [25], there are three basic flavors of scheduling algorithms: namely, the round robin (RR) scheduling, maximum rate (MR) scheduling, and proportional fairness (PF) scheduling. A RR scheduler assigns radio resources to all UEs in a network cell with identical priority, regardless of the channel state experienced by different UEs. In this way, the fairness of resource sharing is maximized. However, it is less efficient in providing UEs with a high data rate. A MR scheduler on the other hand prioritizes UEs conditioned on their channel state. The UEs with high SINR values are served first, and those who suffer from severe channel fading will not be scheduled. As a consequence, the radio resources are unfairly assigned to UEs, but the cell capacity can be maximized. A PF scheduler provides a balance between fairness and efficiency. It tries to fairly schedule UEs while maximizing the system throughput. In such a algorithm, a proportional fairness ratio  $P_k(t)$  is computed for each UE  $k$  and updated at each time scale  $t$  as follows:

$$P_k(t) = \frac{r_k(t)}{R_k(t)} \quad (2.8)$$

the numerator  $r_k(t)$  denotes the instantaneous bit rate that UE  $k$  can be served in the upcoming time snapshot  $t$ . A reasonable approach is to derive  $r_k(t)$  based on single-user MIMO (SU-MIMO) transmission since at this stage it is undecided which UEs will be served. An MRT precoder is applied here to maximize the signal power. In the denominator,  $R_k(t)$  represents the average throughput experienced by UE  $k$  up to and includes time snapshot  $t - 1$ , and it is updated as follows:

$$R_k(t) = (1 - \gamma)R_k(t - 1) + \gamma\hat{R}_k(t - 1) \quad (2.9)$$

herein,  $\gamma$  is the exponential smoothing factor and  $\hat{R}_k(t - 1)$  is the instantaneous bit rate that UE  $k$  experienced at the time snapshot  $t - 1$ . A typical setting of  $\gamma = 0.01$  is assumed, in line with e.g., [28]. At the beginning of the simulation,  $R_k(0)$  is initialized to zero, which implies that every UE has an equal (infinity) PF ratio. In such a case, we apply a tie-breaking rule and order the UEs based on their SU-MIMO throughput  $r_k(0)$ . At other given time scale  $t$ , the PF packet scheduler ranks the UEs conditioned on their PF ratio  $P_k(t)$ . The UE with the highest ratio will be served first. Then, the scheduler goes through other UEs one by one and decides whether it will be scheduled. To achieve this, an adaption of the heuristic semi-orthogonal user selection algorithm is employed as outlined below:

**Algorithm 1:** Adapted semi-orthogonal user selection

---

```

for  $t = 1$  to  $T$  do
  Initialize: candidate UE set  $\mathcal{X}_{CS} = \{1, 2, \dots, K\} - \{k^*\}$  and scheduled UE set
     $\mathcal{X}_{SS} = \{k^*\}$ , where  $k^* = \underset{k \in \{1, 2, \dots, K\}}{\operatorname{argmax}} P_k(t)$ 
  while  $\mathcal{X}_{CS} \neq \emptyset$  do
     $k^* = \underset{k \in \mathcal{X}_{CS}}{\operatorname{argmax}} P_k(t)$ 
    if  $|\mathbf{v}_{l^*,k^*} \mathbf{v}_{l,k}^H| \leq \delta \|\mathbf{v}_{l^*,k^*}\| \|\mathbf{v}_{l,k}\| \forall l^* \in \{1, \dots, L_{k^*}\}, l \in \{1, \dots, L_k\}, k \in \mathcal{X}_{SS}$  then
       $\mathcal{X}_{SS} = \mathcal{X}_{SS} + \{k^*\}$ 
    end
     $\mathcal{X}_{CS} = \mathcal{X}_{CS} - \{k^*\}$ 
  end
end

```

---

In this algorithm, the candidate UE set  $\mathcal{X}_{CS}$  and the scheduled UE set  $\mathcal{X}_{SS}$  are initialized by considering the UE with the highest proportional fairness ratio at the time snapshot  $t$  ( $t \neq 0$ ). The next step checks whether the channels of UE  $k^*$  in the candidate set satisfy the following criterion for all UEs in the scheduled set:

$$|\mathbf{v}_{l^*,k^*} \mathbf{v}_{l,k}^H| \leq \delta \|\mathbf{v}_{l^*,k^*}\| \|\mathbf{v}_{l,k}\| \quad (2.10)$$

where the channel vector  $\mathbf{v}_{l,k}$  corresponding to layer  $l$  of UE  $k$  that is already scheduled. The idea is to select a candidate UE that has sufficiently uncorrelated channels compared to already scheduled UEs. Herein, the sufficiency is characterized by a configuration parameter  $\delta \in [0, 1]$ . Two extreme cases are  $\delta = 0$  and  $\delta = 1$ . For  $\delta = 0$ , this check is never fulfilled, and only the UE  $k^*$  is served at each TTI (SU-MIMO). At the other extreme, all UEs end up being scheduled all the time. In between these extremes,  $\delta$  can be optimally tuned to enlarge cell capacity. Under the assumption of fixed-layer transmission, a candidate UE  $k^*$  is served only if all its  $L_{k^*}$  layers can be scheduled. Finally, after co-scheduling the UEs at each time snapshot, the sum system throughput can be determined by performing the Beamforming block and the Link-to-System Mapping block.

## 2.6. Integration of Individual Blocks

So far, four individual blocks and two radio resource management schemes are introduced. In the section, these blocks and schemes are integrated to formulate the complete system model as shown in Figure 2.7. An overview of the 5G NR SLS model is provided here. First, the QuaDRiGa antenna parameters are generated using the statistical environment information. Afterward, the channel matrix is computed in the QuaDRiGa radio channel generator. Under the assumption of single-user transmission, the Beamforming and Link-to-System Mapping blocks can be performed to derive the numerator of the proportional fairness ratio. The denominator of the proportional fairness ratio is updated at each time snapshot based on the instantaneous bit rate experienced by the UEs. After ranking the UEs conditioned on their proportional fairness ratio, an adapted semi-orthogonal user selection algorithm is applied to co-schedule the UEs that have sufficiently uncorrelated channels. Lastly, the Beamforming and Link-to-System Mapping blocks are implemented again to predict the system performance based on the statistical system throughput.

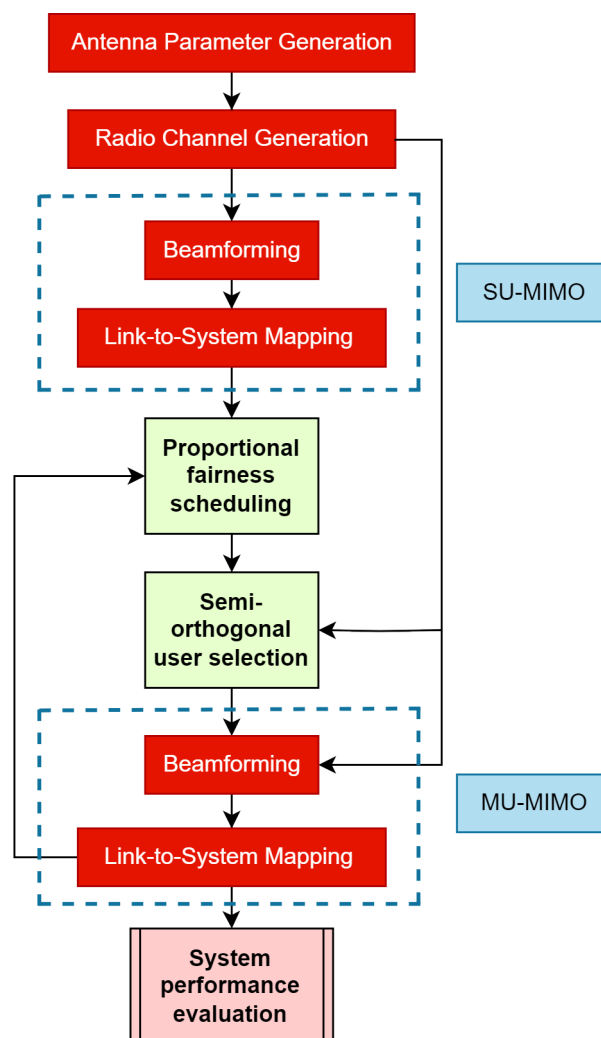


**Figure 2.7:** Schematic of the 5G NR SLS model

# 3

## Simulation Setting

In this chapter, the layout of the cellular radio network and four spatially heterogeneous user distributions are presented in Section 3.1. Following this, Section 3.2 proposes two hybrid beamforming architectures with subarray beam pattern shaping. Two benchmark antenna structures with fully digital beamforming and hybrid beamforming respectively are generated for comparison. Lastly, the overall parameter setup in QuaDRiGa is shown in Section 3.3.

### 3.1. Network Layout and User Distributions

The use of directional antennas allows a site (equipped with multiple panels) to serve multiple sectors. The most common and efficient way of cell division is to split it into three hexagonal sectors. In this research, a single base station is deployed to serve UEs in one sector of a three-sectorized site. Under the standardization of 3GPP NR channel models for urban macro (UMa) cell [30], the base station antenna height is set as 25 meters, the height of UE is set as 1.5 meters, and the intersite distance (ISD) is configured as 500 meters. As a result, the cell range (the length of the diagonal of a hexagonal sector) is calculated as 333 meters. An approximation of user distribution is made by placing the UEs inside the red circle inscribing the hexagonal sector, as visualized in Figure 3.1. In such a way, a minimum distance of 22 meters can be guaranteed to avoid users being too close to the base station and exposed to strong harmful near-field radiations.

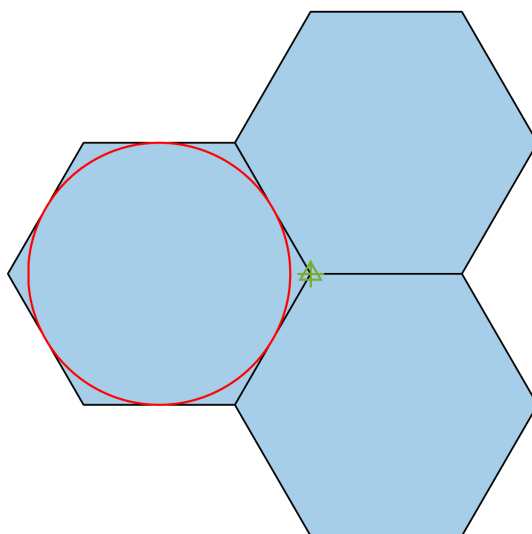


**Figure 3.1:** Layout of a three-sectorized site

To configure spatially heterogeneous user distribution scenarios, the percentage of UEs  $\eta$  with respect to the antenna downtilt angle  $\theta$  is computed. Herein, the UEs are configured uniformly distributed within the sector (approximated with the red circle), as plotted in Figure 3.2. The calculation is based on the intersection area  $A_{r_1 \cap r_2}$  between the red circle (with radius  $r_1$ ) and the green circle (with radius  $r_2$  and centered at the base station). Moreover, the percentage of uniformly distributed UEs can be derived via the following form:

$$\eta(\theta) = \frac{A_{r_1} - A_{r_1 \cap r_2}(\theta)}{A_{r_1}} \quad (3.1)$$

the result is plotted in Figure 3.3. Herein,  $\theta \in [0^\circ, 90^\circ]$  covers the region below the horizon up until the base station. In the figure, three annotations correspond to different antenna downtilt angles and user distribution percentages. The first one represents the cell edge users at an angle of  $4^\circ$ . Followed by the angle  $15^\circ$  that includes 90% of the users. The boundary of 90% user distribution is visualized by the green arc in Figure 3.2. The last one shows that all of the users are distributed within an angle of  $46^\circ$  from the cell edge.

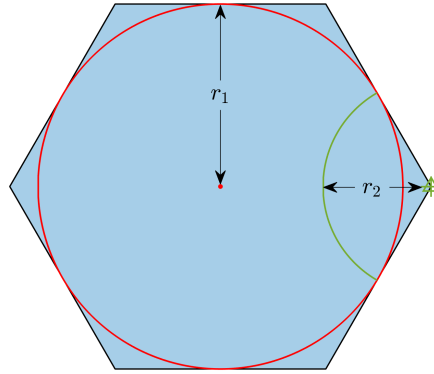


**Figure 3.2:** Uniform user distribution

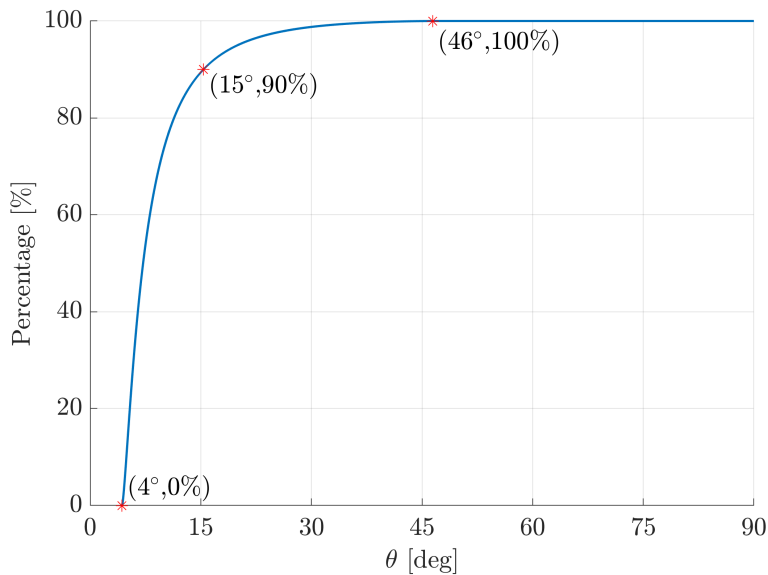


**Figure 3.3:** Percentage of uniformly distributed users as a function of the antenna downtilt angle

Based on the analysis of uniform user distribution, three non-uniform spatial traffic distributions are created in Figure 3.4. In these cases, the users are placed within different locations of the hot spot. This can represent the traffic flow and mobility of users due to festivals and holidays. In Figure 3.4a, the small red circle intersects the green circle and the big red circle, corresponding to the antenna downtilt angle  $\theta \in [15^\circ, 46^\circ]$ . The second case places the users around the cell center, with the angle  $\theta$  varying from  $7^\circ$  to  $10^\circ$ . In the last scenario, the users are distributed near the cell edge and stand for the range of  $\theta$  between  $4^\circ$  and  $5^\circ$ .

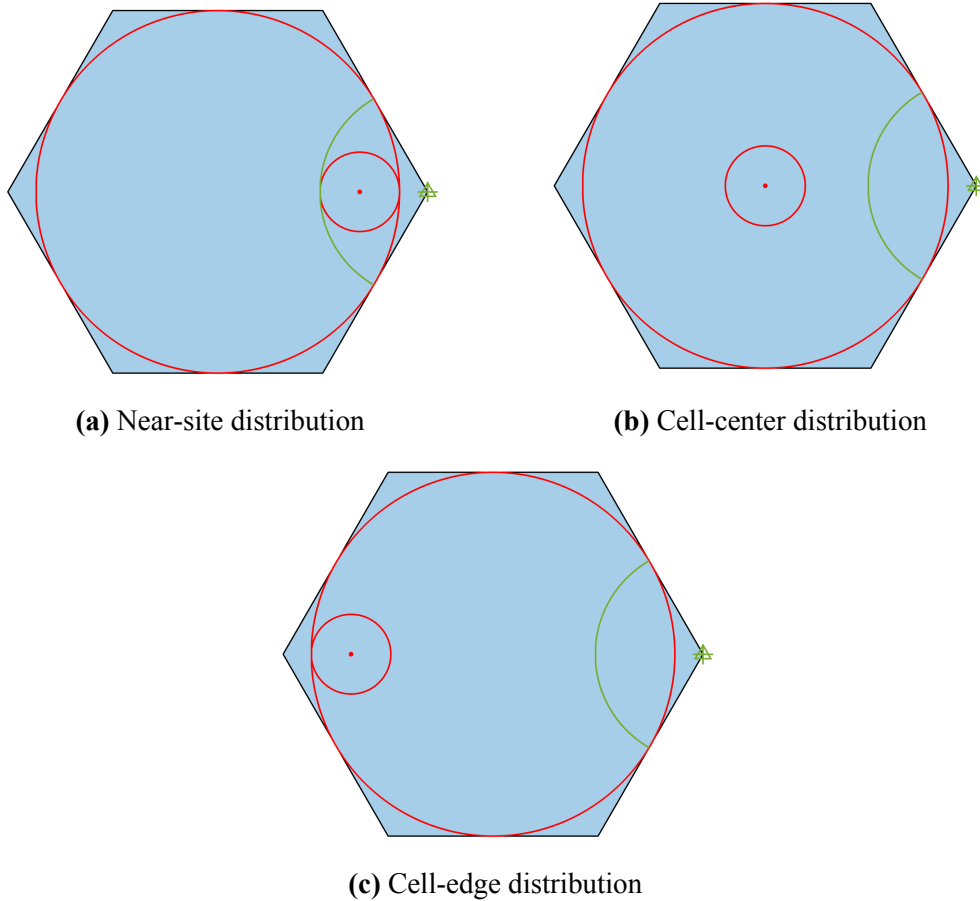


**Figure 3.4:** Three non-uniform user distributions

## 3.2. Beamforming Architectures

In the previous section, the network layout and heterogeneous user distribution scenarios are introduced. Based on that, two HBF approaches with shaped subarray beam patterns are proposed. Before synthesizing the desired patterns, the benchmark antenna structure with fully digital beamforming is generated. The benchmark DBF antenna array is composed of  $12 \times 16 \times 2$  antenna elements with a half-wavelength elements spacing. The antenna elements are vertically and horizontally polarized. Such an array antenna topology is shown in Figure 3.5.

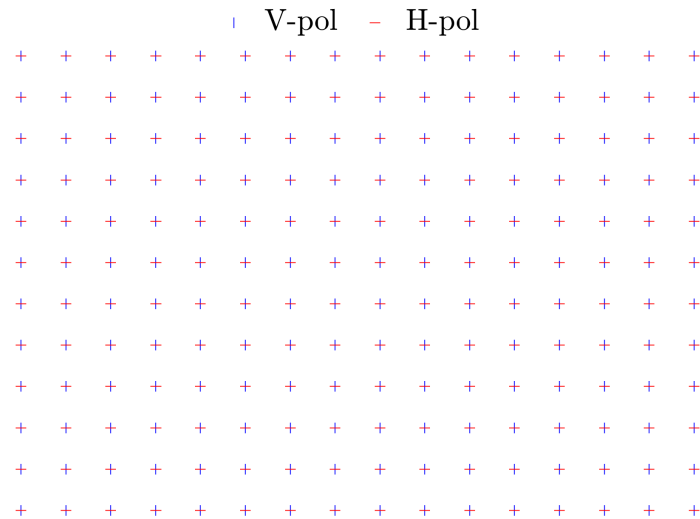


**Figure 3.5:** Array antenna topology of benchmark DBF

The slot antenna element used in different beamforming architectures is designed in CST Studio Suite driven by studies [12], [13], [41], as presented in Figure 3.6. Herein, the transverse slot is fed by the substrate-integrated waveguide (SIW), and it can realize the vertical polarization of transmit waves. A tapered distribution in amplitude is controlled by the length of the slot, and the phase delay is modified through the width of the phase element. There is also a pair of vias added to the SIW for reflection-canceling. Such a structure can be applied to the design of HBF architectures and provides the wanted subarray antenna pattern.

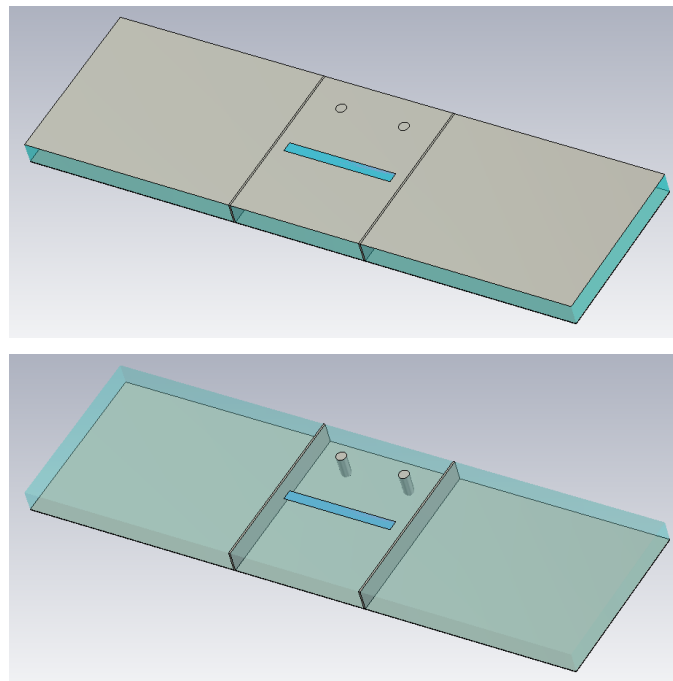


**Figure 3.6:** Structure of the slot antenna element

Note that the unit slot antenna is designed with vertical polarization in SIW technology, which makes the realization of a dual-polarized antenna array more complex. Alternatively, the antenna dual-polarization is modeled in QuaDRiGa in the following procedures. First, the 3D field pattern of the slot antenna element is exported from CST Studio Suite and converted to a QuaDRiGa antenna object. As a result, the 2D antenna pattern at  $\phi = 0^\circ$  cut is plotted in Figure 3.7. From the graph, the maximum gain is achieved around 6 dBi at  $\theta = 0^\circ$ . Afterward, the co-polarized and cross-polarized parts of the 3D antenna pattern are presented in Figure 3.8. To model the antenna dual-polarization, the horizontal polarization is created from the vertically-polarized slot antenna with the same pattern and at the same location, only their polarization is the opposite. This can be regarded as an idealized modeling of the antenna dual-polarization since the mutual coupling effect among distinct antenna elements is ignored.

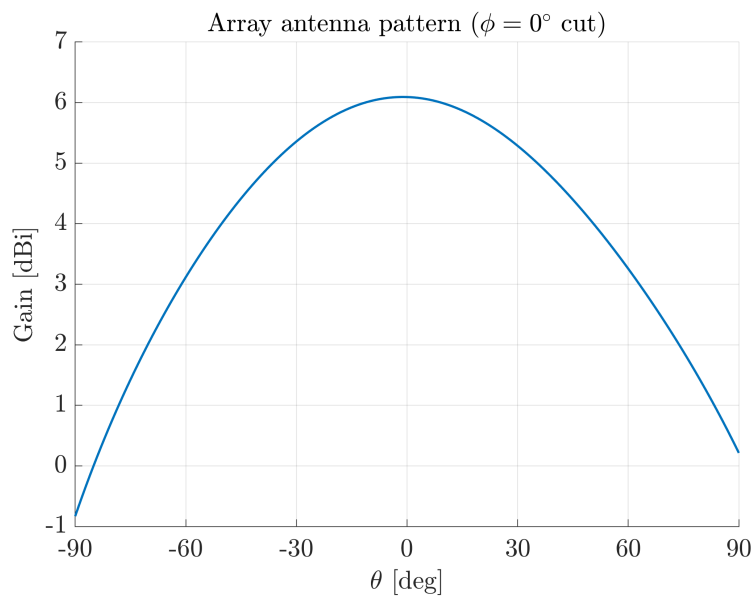


**Figure 3.7:** 2D pattern of the slot antenna element at  $\phi = 0^\circ$  cut

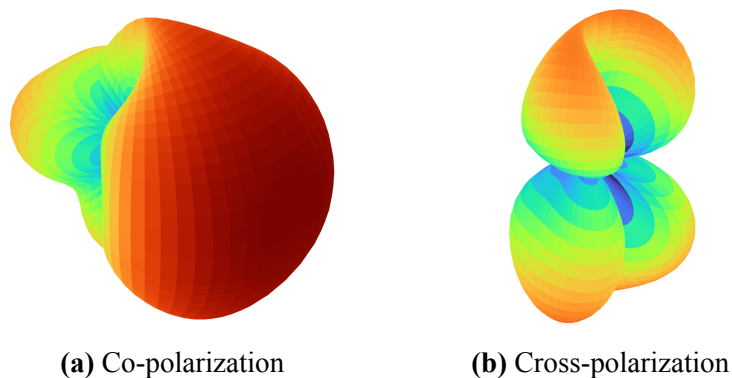


**Figure 3.8:** 3D pattern of the slot antenna element

After generating the benchmark DBF antenna array, two HBF architectures with shaped beam patterns in elevation are proposed. The array topology of such an HBF method is shown in Figure 3.9, where the antennas in the elevation direction are grouped into subarrays. Each subarray can be considered as one antenna object. There are in total 32 subarrays and they are dual-polarized as well.

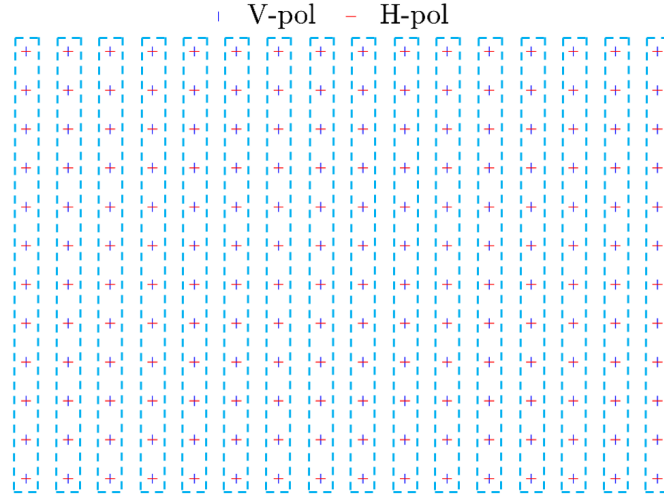


**Figure 3.9:** Array antenna topology of HBF structures

The synthesis of a cosecant-squared pattern and a flat-top pattern is plotted in Figure 3.10. The cosecant-squared pattern is designed to achieve a high gain (approx. 12 dBi) at the cell edge (i.e.,  $\theta = 4^\circ$ ), and compensate for severe signal attenuation at the mm-Wave spectrum. From the cell edge to the base station (i.e.,  $\theta \in [4^\circ, 46^\circ]$ ), the gain is exponentially decreased. In such a pattern, the received power is equalized for users at different ranges, the interfering radiation toward the neighboring cells and above the horizon (e.g., drones, airplanes, and high-rise buildings) is minimized, and safety issues related to vertical compliance distance (see e.g., [14]) are avoided. In the flat-top pattern, the gain is averaged (approx. 11 dBi) for different users regardless of their channel conditions. Consequently, the cosecant-squared pattern focuses on cell edge users while the flat-top pattern treats all the users equally.

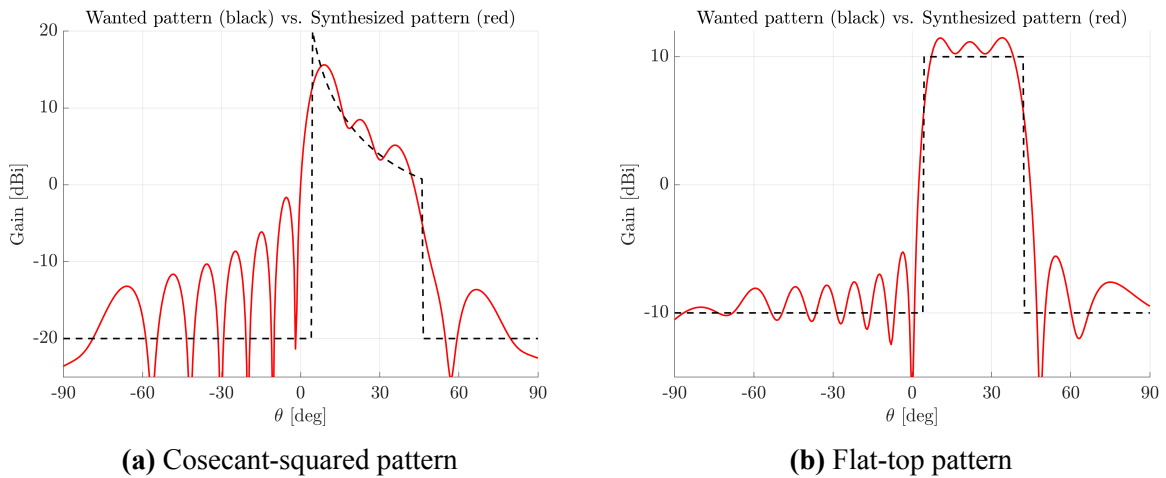


**Figure 3.10:** Synthesis of proposed subarray beam patterns

After the beam pattern synthesis, the array factor of each subarray antenna is input to CST Studio Suite, and the 3D subarray antenna pattern is generated. Following the same modeling step as benchmark DBF, the antenna parameters are produced in QuaDRiGa. As a result, the co-polarized and cross-polarized parts of HBF antennas with a cosecant-squared pattern and a flat-top pattern are visualized in Figure 3.11 and 3.12 respectively.

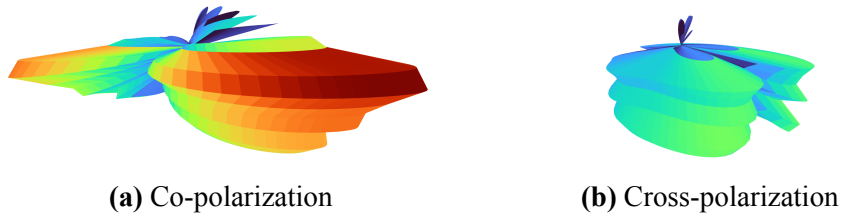


**Figure 3.11:** 3D subarray antenna pattern of HBF with cosecant-squared shaping

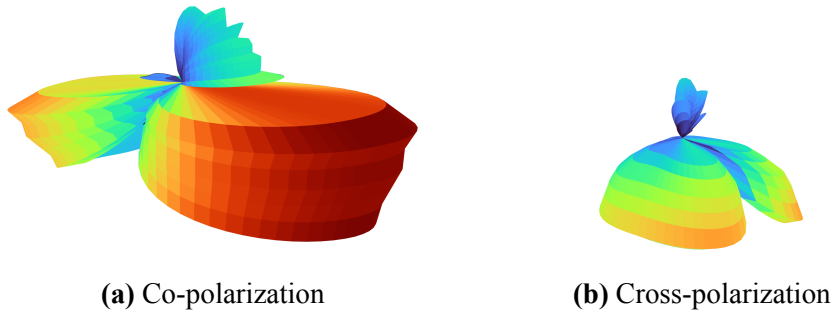


**Figure 3.12:** 3D subarray antenna pattern of HBF with flat-top shaping

To compare with shaped HBF antenna arrays, the benchmark HBF architecture is generated with the same topology in Figure 3.9. The antenna elements inside the subarrays of benchmark HBF are fed with the same amplitude, their phases are weighted such that the main beam is shifted toward the cell edge. The 2D and 3D subarray antenna pattern of benchmark HBF is plotted in Figure 3.13 and 3.14 respectively. In addition, the 2D subarray antenna patterns of shaped HBF and benchmark HBF structures are plotted altogether in Figure 3.15.

In summary, four different beamforming architectures are generated in this section, i.e., HBF with a cosecant-squared pattern, HBF with a flat-top pattern, benchmark HBF, and benchmark DBF. They share the same unit slot antenna and are horizontally and vertically polarized. In the next section, the overall parameter setup in QuaGRiGa will be displayed.

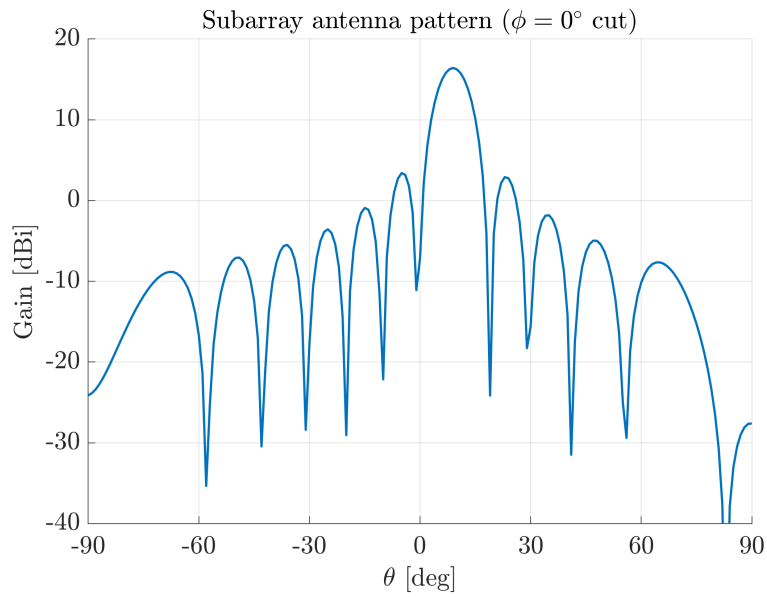


**Figure 3.13:** 2D subarray antenna pattern of benchmark HBF at  $\phi = 0^\circ$  cut



**Figure 3.14:** 3D subarray antenna pattern of benchmark HBF

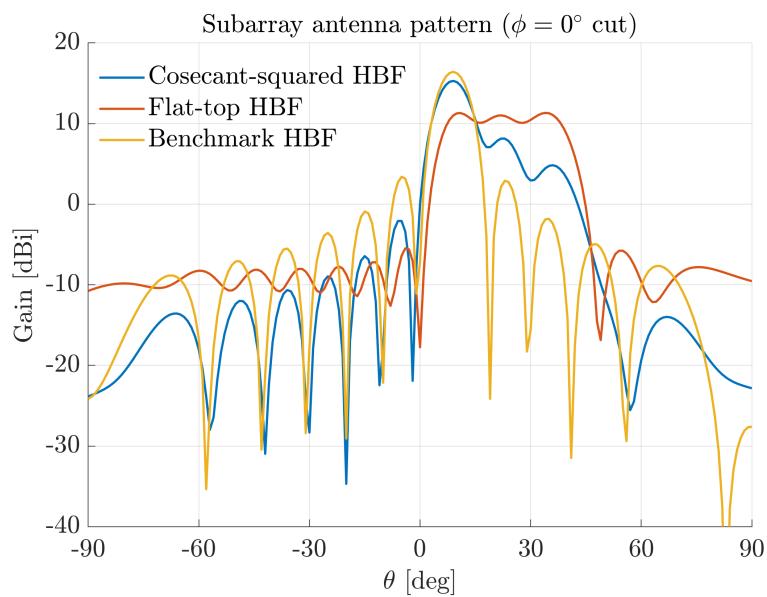


**Figure 3.15:** 2D subarray antenna pattern of different HBF structures at  $\phi = 0^\circ$  cut

### 3.3. QuaDRiGa Parameter Setup

The parameter setup in QuaDRiGa in line with the Radio Channel Generation block (see Section 2.2) of the SLS model is presented in this section. The overall setting is separated into four parts, i.e., the base station parameters, the UE parameters, the network parameters, and the propagation scenarios.

The base station is equipped with the antenna models as introduced in Section 2.3, with 25 meters height and a transmitted power of 188 watts (based on per-antenna radiated power). An example of the base station parameter setup with the benchmark DBF beamforming architecture is shown in Table 3.1.

The UE uses the antenna model under the 3GPP-3D channel model as defined in [29]. It is configured by a dual-polarized  $2 \times 2$  planar array at a height of 1.5 meters. In addition, to model the time evolution of channels, the UE is assumed to linearly move at a speed of 3 km/h in a random direction. An overview of the UE parameter setting can be found in Table 3.2.

The network parameters are shown in Table 3.3. Herein, the carrier frequency is set to 26 GHz (FR2). The carrier bandwidth is configured as 36 MHz with 50 PRBs and 60 kHz subcarrier spacing. Such a 5G PRB block and a resource element (the smallest physical channel unit) are visualized in Figure 3.16. Given the computational complexity and the limitation of data storage, the number of TTIs is set to 10 in the simulation. Note that the choice of TTIs is too few to properly apply the PF scheduling algorithm, which can be improved for future research.

Under the 3GPP standardization [30], the 3GPP NR channel models for urban macro (UMa) cell are selected with LoS and NLoS propagations. It is noticeable that the LoS and NLoS scenarios here are both with multipath propagations.

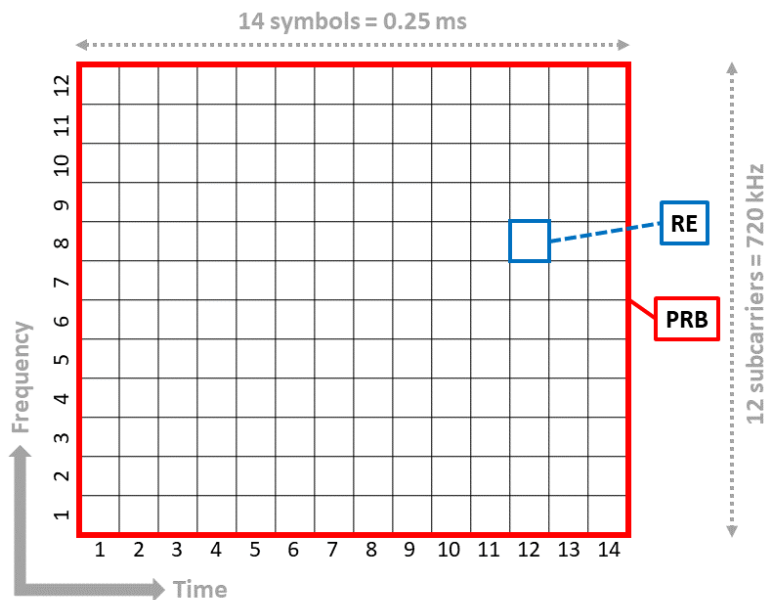


**Figure 3.16:** A 5G physical resource block (PRB) block and a resource element (RE) with 60 kHz subcarrier spacing

| Base station parameter            | Value         |
|-----------------------------------|---------------|
| Height in [m]                     | 25            |
| Antenna model                     | Benchmark DBF |
| Vertical size                     | 12            |
| Horizontal size                   | 16            |
| Polarization                      | H/V           |
| Elements spacing in [ $\lambda$ ] | 0.5           |
| Number of antenna elements        | 384           |
| Transmitted power in [W]          | 188           |

**Table 3.1:** An example of the base station parameter setup in QuaDRiGa with the benchmark DBF antenna model

| UE parameter                      | Value   |
|-----------------------------------|---------|
| Height in [m]                     | 1.5     |
| Speed in [km/h]                   | 3       |
| Antenna model                     | 3GPP-3D |
| Vertical size                     | 2       |
| Horizontal size                   | 2       |
| Polarization                      | H/V     |
| Elements spacing in [ $\lambda$ ] | 0.5     |
| Number of antenna elements        | 8       |

**Table 3.2:** UE parameter setup in QuaDRiGa

| Network parameter           | Value |
|-----------------------------|-------|
| Cell range in [m]           | 333   |
| Carrier frequency in [GHz]  | 26    |
| Subcarrier spacing in [kHz] | 60    |
| Carrier bandwidth in [MHz]  | 36    |
| Number of PRBs              | 50    |
| Number of TTIs              | 10    |

**Table 3.3:** Network parameter setup in QuaDRiGa

# 4

## Results and Discussion

In this chapter, the rank strategy is selected to fix the number of transmission layers in Section 4.1. Section 4.2 motivates the reason for configuring the user selection scheme based on the number of users. Lastly, the system performance variation of deploying diverse beamforming architectures in heterogeneous user distributions and different propagation scenarios is evaluated in Section 4.3.

### 4.1. Rank Strategy Selection

In this section, the motivation for choosing the fixed-rank 2 (R2) strategy is discussed. Herein, the fixed-rank 1 (R1) and fixed-rank 4 (R4) strategies are added for comparison. We consider a total number of 10 UEs ( $K = 10$ ) that are uniformly distributed within the cell (see Figure 3.2). LoS propagation is assumed and we simulate 1000 snapshots. In each simulation snapshot, the UEs have random positions and movement directions, and the scatterers are randomly spaced as well. The simulation parameters are summarized in the following table.

| Simulation parameter           | Value           |
|--------------------------------|-----------------|
| Antenna model                  | Benchmark DBF   |
| User distribution              | Uniform         |
| Rank                           | {1, 2, 4}       |
| Number of UEs                  | 10              |
| Number of simulation snapshots | 1000            |
| Channel model                  | 3GPP NR UMa LoS |

**Table 4.1:** Simulation parameters for the rank strategy selection

After applying the SLS model based on the above simulation parameters, the bit rates with different rank strategies are obtained. First, the performance is analyzed at the user level. Namely, the percentage over the users and time/simulation snapshots for which R1/R2/R4 yields the highest bit rate is shown in Figure 4.1. From the figure, no fixed-rank strategy always has the best performance (i.e., 100%). This indicates that the rank strategy is ideally adapted at each time snapshot, which is indeed what is done in practical implementations. However, in this study, we choose to follow a fixed-rank strategy for implementational simplicity. Given this modeling choice, the results in Figure 4.1 suggest that it is best to opt for the rank 2 strategy since it has the highest percentage (approx. 49%) and outperforms the other two.

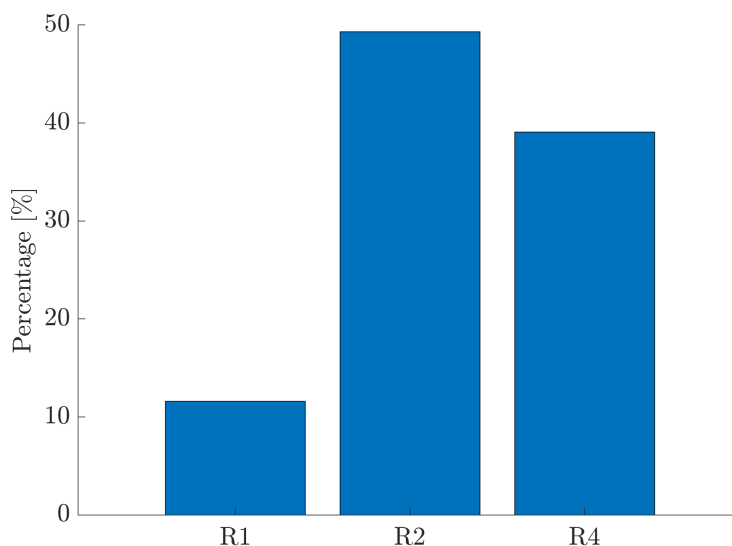


**Figure 4.1:** Comparison of different fixed-rank strategies at the user level

Next, the performance is compared at the system level. Herein, the percentage over simulation snapshots for which fixed-rank strategy outputs the highest time-averaged cell throughput is plotted in Figure 4.2. It is observed that the rank 2 strategy again has better performance (63.6%) than rank 1 (0%) and rank 4 (36.4%) strategies. In conclusion, the system gains the most from splitting the power over two transmission layers than no power splitting and four-layer power splitting. Based on the user and system perspectives, the fixed-rank 2 strategy is chosen for the rest of the simulations.

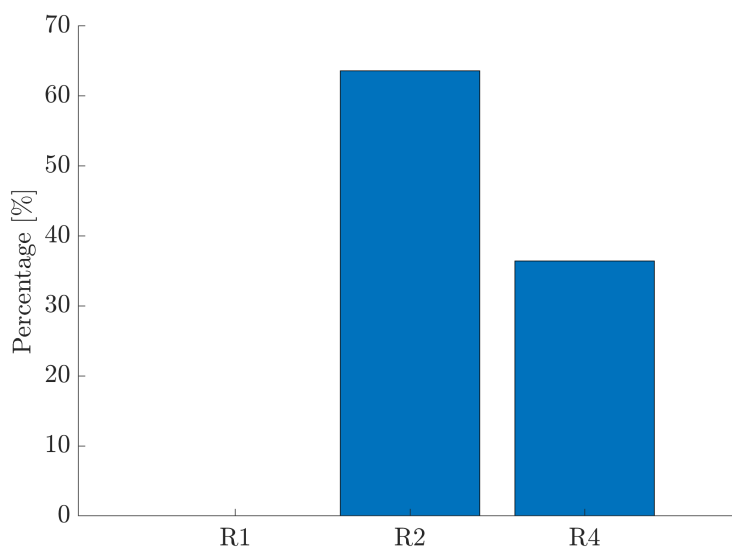


**Figure 4.2:** Comparison of different fixed-rank strategies at the system level

## 4.2. User Selection Scheme Configuration

In Section 2.6, it is mentioned that the proportional fairness scheduling and an adapted semi-orthogonal user selection algorithm are adopted to schedule users at each time snapshot. Moreover, the threshold  $\delta$  in Equation 2.10 checks the channel orthogonality of candidate UEs versus already scheduled UEs. To explore the effect of varying  $\delta$  values, the system performance is simulated with  $\delta \in \{0, 0.1, \dots, 1\}$  (an interval of 0.1) and different numbers of UEs  $K \in \{10, 50, 100, 150\}$ . The simulation parameters can be found in Table 4.2. Herein, the number of transmission layers (rank) is fixed to 2 and the number of simulation snapshots is set as 100 (considering the computational complexity for  $K \in \{50, 100, 150\}$ ).

| Simulation parameter           | Value                  |
|--------------------------------|------------------------|
| Antenna model                  | Benchmark DBF          |
| User distribution              | Uniform                |
| Rank                           | 2                      |
| $\delta$                       | $\{0, 0.1, \dots, 1\}$ |
| Number of UEs                  | $\{10, 50, 100, 150\}$ |
| Number of simulation snapshots | 100                    |
| Channel model                  | 3GPP NR UMa LoS        |

**Table 4.2:** Simulation parameters for the user selection scheme optimization

The simulation results are discussed here. Note that in the following analysis, the time-averaged user/system throughput is averaged over simulation snapshots. First, the average user throughput versus the threshold  $\delta$  for different numbers of UEs is plotted in Figure 4.3. From the figure, it is observed that for a higher  $K$ , the average per-user throughput is lower. This is caused by the equal power sharing among the transmission layers of different UEs.

Next, the system throughput with different  $\delta$  values and number of UEs is presented in Figure 4.4. In addition, the optimal  $\delta$  value when the system achieves the best performance is marked with a circle for each curve. In the case of 10 UEs, the optimal  $\delta$  value is 1, which suggests that all UEs can be served all the time without having much interuser interference. By increasing the number of UEs to 50, the optimal  $\delta$  is shifted to 0.7. It is further reduced to 0.4 when there are 100 and 150 UEs in the cell. The above observations indicate that if the users are separated well enough (i.e., when  $K = 10$ ), the interuser interference is insignificant. On average over simulation snapshots, the system gains the most by scheduling all UEs at each TTI. If considering a large number of UEs (i.e., when  $K \in \{50, 100, 150\}$ ), the interuser interference becomes dominant and hugely affects the system performance. To cope with this issue, the base station can schedule its transmission to those users with favorable channel fading conditions and improve the system performance. This is due to the multiuser diversity effect. The SUS user selection scheme tries to smartly schedule the users conditioned on their channel status and optimize the degree of MU-MIMO by configuring the threshold  $\delta$  for a fixed  $K$ . As a result, for a higher  $K$ , the best-achieved system throughput is increased at the cost of computational complexity. In addition, the choice of optimal  $\delta$  depends on the number of users, which suggests a dynamic adaption of the user selection scheme in a real system with a time-varying  $K$ . After the optimal  $\delta$  for 50, 100, and 150 UEs, the system does not

gain from the multiuser diversity effect anymore. Moreover, the system throughput drop from the optimal  $\delta$  to  $\delta = 1$  is much higher for a larger  $K$  due to the significance of interuser interference, which results in three curves crossing each other.

To sum up, the impact of configuration parameter  $\delta$  in the SUS user selection algorithm with varying numbers of UEs is analyzed in this section. In the presence of a large number of UEs, the system gains from the multiuser diversity effect by scheduling the users with favorable channel conditions. Furthermore, it is motivated to configure the threshold  $\delta$  with a varying number of users to enhance the system performance.

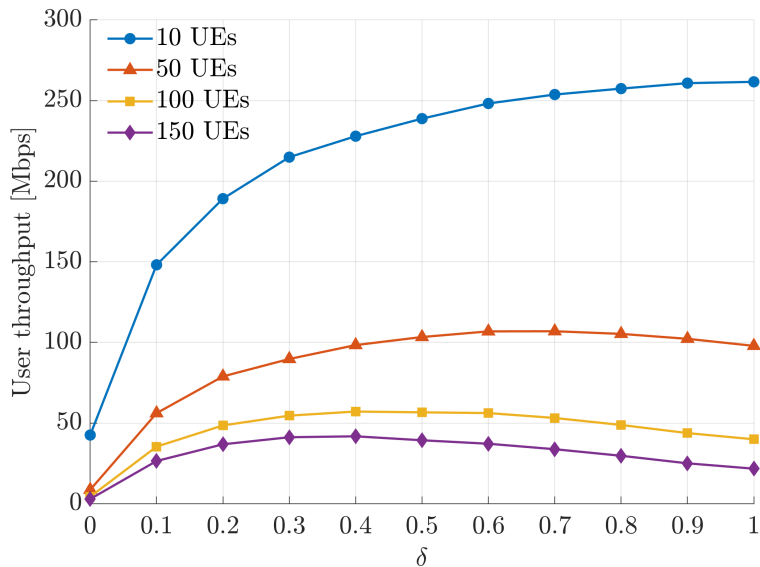


**Figure 4.3:** Average user throughput versus the threshold  $\delta$

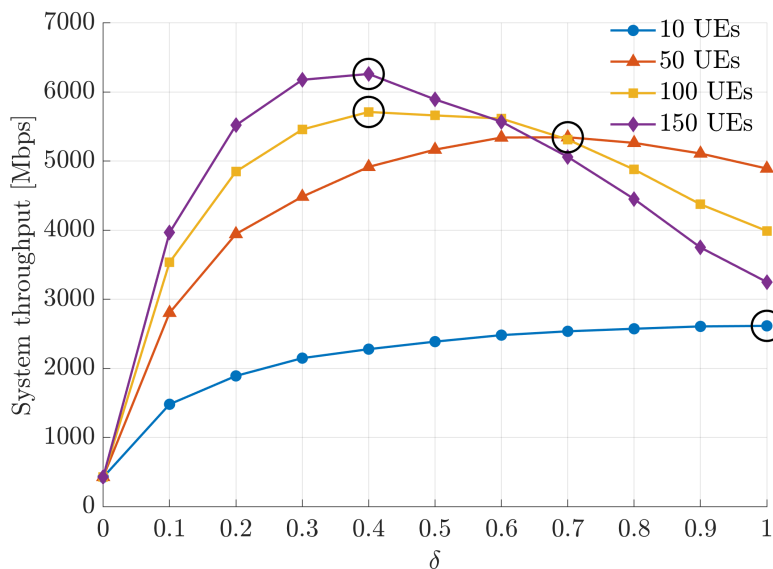


**Figure 4.4:** System throughput versus the threshold  $\delta$

### 4.3. System Performance Evaluation

After fixing the rank strategy to use two transmission layers per UE and having decided to configure the  $\delta$  parameter of the user selection scheme based on the number of users, the system performance of deploying various beamforming structures in uniform/non-uniform user distributions and LoS/NLoS propagation scenarios is evaluated in this section. Note that for a fair comparison, the threshold  $\delta$  is optimally configured for each number of users, beamforming structure, user distribution, and propagation scenario. The simulation results under the line-of-sight and non-line-of-sight propagations are discussed separately in Section 4.3.1 and 4.3.2. Particularly, the performance variation of having different numbers of UEs (i.e.,  $K \in \{10, 20\}$ ) is analyzed in the LoS scenario. The simulation parameters are shown in the following table.

| Simulation parameter           | Value  |
|--------------------------------|--|
| Antenna model                  | {Cosecant-squared HBF, flat-top HBF, benchmark HBF, benchmark DBF} |
| User distribution              | {Uniform, near-site, cell-center, cell-edge}                       |
| Rank                           | 2  |
| Number of UEs                  | {10, 20}   |
| Number of simulation snapshots | 1000   |
| Channel model                  | 3GPP NR UMa LoS/NLoS   |

**Table 4.3:** Simulation parameters for the system performance evaluation

#### 4.3.1. Line-of-Sight Scenario

The simulation results under the LoS propagation are discussed here (see Appendix A for the CDF curves and 10th percentile CDF values). To start with, the number of UEs is set to 10 and they are uniformly distributed within the cell (see Figure 3.2). For each simulation snapshot and beamforming approach, the time-averaged system throughput is computed using the SLS model. Afterward, the cumulative distribution function (CDF) of the system throughput for different beamforming architectures is plotted in Figure 4.5. It is observed from the figure that the benchmark DBF outperforms the other three HBF beamforming methods. The reason is that the DBF approach has full beamforming flexibility and is able to produce 3D adaptive beams, while the three considered fixed subarray HBF alternatives can only steer the beam in the azimuth plane. The trade-offs between them lie in although DBF beamforming brings significant gain in system performance, it also costs much more computational resources and is complex in the RF front-end structure.

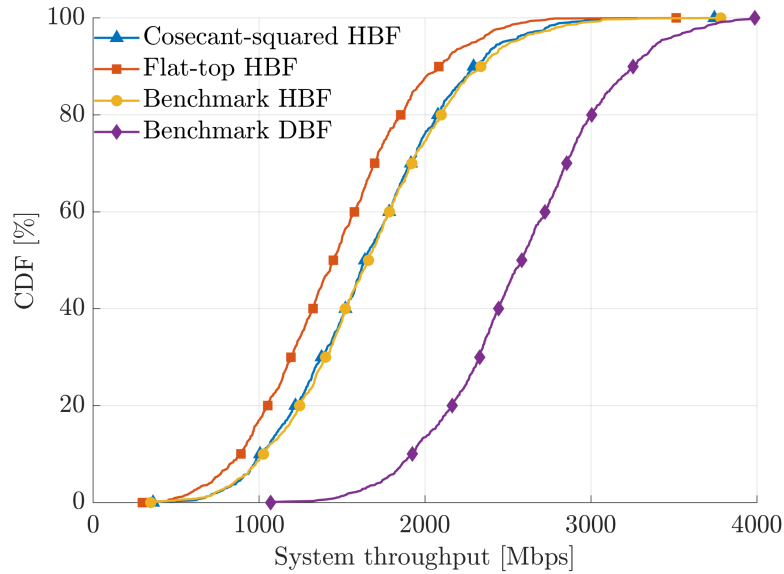


**Figure 4.5:** CDF curves for different beamforming architectures with uniformly distributed 10 UEs under the LoS scenario

From the CDF curves, the cosecant-squared HBF has similar performance compared to the benchmark HBF, and they both outperform the flat-top HBF. Commonly, the network operators take the 10th percentile CDF value as an important system performance evaluation metric as it can be interpreted to reflect the cell edge performance. By using 10th percentile CDF values, the performance of shaped HBF structures versus benchmarks is presented in Figure 4.6. Herein, Figure 4.6a shows the 10th percentile system throughput, and Figure 4.6b plots the gain of having shaped HBF methods over the benchmarks. The results illustrate that the cosecant-squared HBF performs slightly worse ( $-2\%$ ) than the benchmark HBF under the assumed uniform user distribution and LoS scenario, while the flat-top HBF has a considerable performance degradation ( $-13.2\%$ ). The system performance of the cosecant-squared HBF and flat-top HBF is significantly dropped by 47.7% and 53.7% respectively compared to the benchmark DBF.

The results show that there is no potential improvement in shaping the subarray beam pattern of the HBF antenna for uniform user distribution and the LoS scenario. From the 2D subarray antenna patterns in Figure 3.15 and the percentage of uniform user distribution in Figure 3.3, roughly 90% of the users are served with higher antenna gain by using the benchmark HBF than shaped HBF methods. Particularly, the antenna gain difference over the benchmark HBF is larger for the flat-top HBF than the cosecant-squared HBF. This explains why the cosecant-squared HBF has a better performance than the flat-top HBF but slightly-worse performance than the benchmark HBF. For the rest of the 10% users, the cosecant-squared HBF and flat-top HBF has higher antenna gain than the benchmark HBF, and thus shaped HBF approaches are expected to bring performance improvement for the near-site traffic.

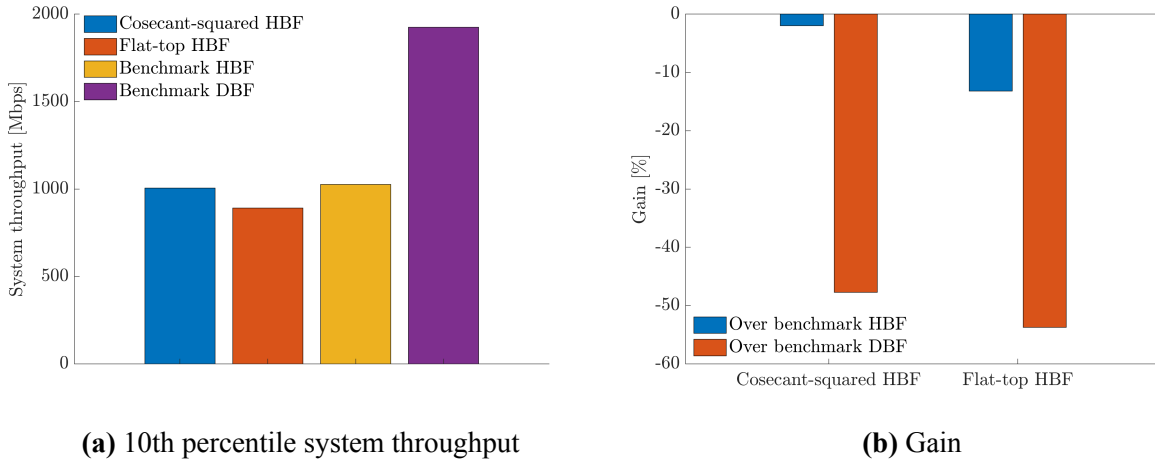


**Figure 4.6:** Comparison of shaped HBF structures and benchmarks with uniformly distributed 10 UEs under the LoS scenario

Next, the system performance is simulated in three cases of non-uniform user distribution (see Figure 3.4). The CDF curves for the case with 10 UEs and LoS scenario are plotted in Figure 4.7. Similar to the uniform user distribution, a significant performance improvement when using the DBF approach is observed in all cases. Therefore, the trade-offs between HBF and DBF beamforming structures in terms of the system performance and computational/RF hardware complexity are again demonstrated here.

The performance comparison between shaped HBF structures and benchmarks with non-uniformly distributed users is presented in Figure 4.8. Herein, the left figure shows the 10th percentile system throughput, and the right figure plots the gain in percentage. From Figure 4.8a, the system performance has been considerably improved over the benchmark HBF with subarray beam pattern shaping for the near-site distribution. Specifically, a gain of 20.6% is achieved using the cosecant-squared HBF and there is 35.3% performance improvement with the flat-top HBF. This indicates that using a flat-top pattern is more beneficial than a cosecant-squared pattern if the users are close to the site, in line with the expectation from their antenna patterns. In the cell-center and cell-edge distributions, the cosecant-squared HBF performs slightly worse than the benchmark HBF ( $-2.9\%$  and  $-2.7\%$  for the cell-center and cell-edge distributions respectively) and there is more performance degradation with the flat-top HBF ( $-14.8\%$  and  $-19.6\%$  for the cell center and cell edge distributions respectively). Compared with the benchmark DBF, a significant performance drop in using shaped HBF architectures is observed. In particular, the performance drop is the highest in the near-site distribution ( $-63.1\%$  and  $-58.6\%$  for the cosecant-squared HBF and flat-top HBF respectively). In the other two distributions, there is less performance decrement ( $-47.5\%$  and  $-53.9\%$  for the cell-center distribution,  $-43.7\%$  and  $-53.5\%$  for the cell-edge distribution).

Another observation from Figure 4.8 is that when the users are distributed further away from the base station (near cell  $\rightarrow$  cell center  $\rightarrow$  cell edge), the system throughput is decreased for all beamforming architectures. This is caused by the severe signal attenuation of mm-Waves. If comparing the uniform and near-site distributions, when the users are closer to the base station and experiencing better channels, the performance of benchmark DBF (1924 Mbps  $\rightarrow$  2247 Mbps) and flat-top HBF (890 Mbps  $\rightarrow$  930 Mbps) is improved. On the contrary, performance degradation of

177 Mbps and 339 Mbps exists for the cosecant-squared HBF and benchmark HBF respectively. It means that the improved channel quality does not bring performance benefits. One reason for the performance drop is that the reduction in antenna gain (as seen in Figure 3.15) dominates over the improvement in channel quality. Another reason could be that the users are placed within a smaller area compared to the uniform user distribution, the elevation and azimuth separation of these users may not be well enough. As a result, fewer users are likely scheduled on average and thus the system performance is not improved.

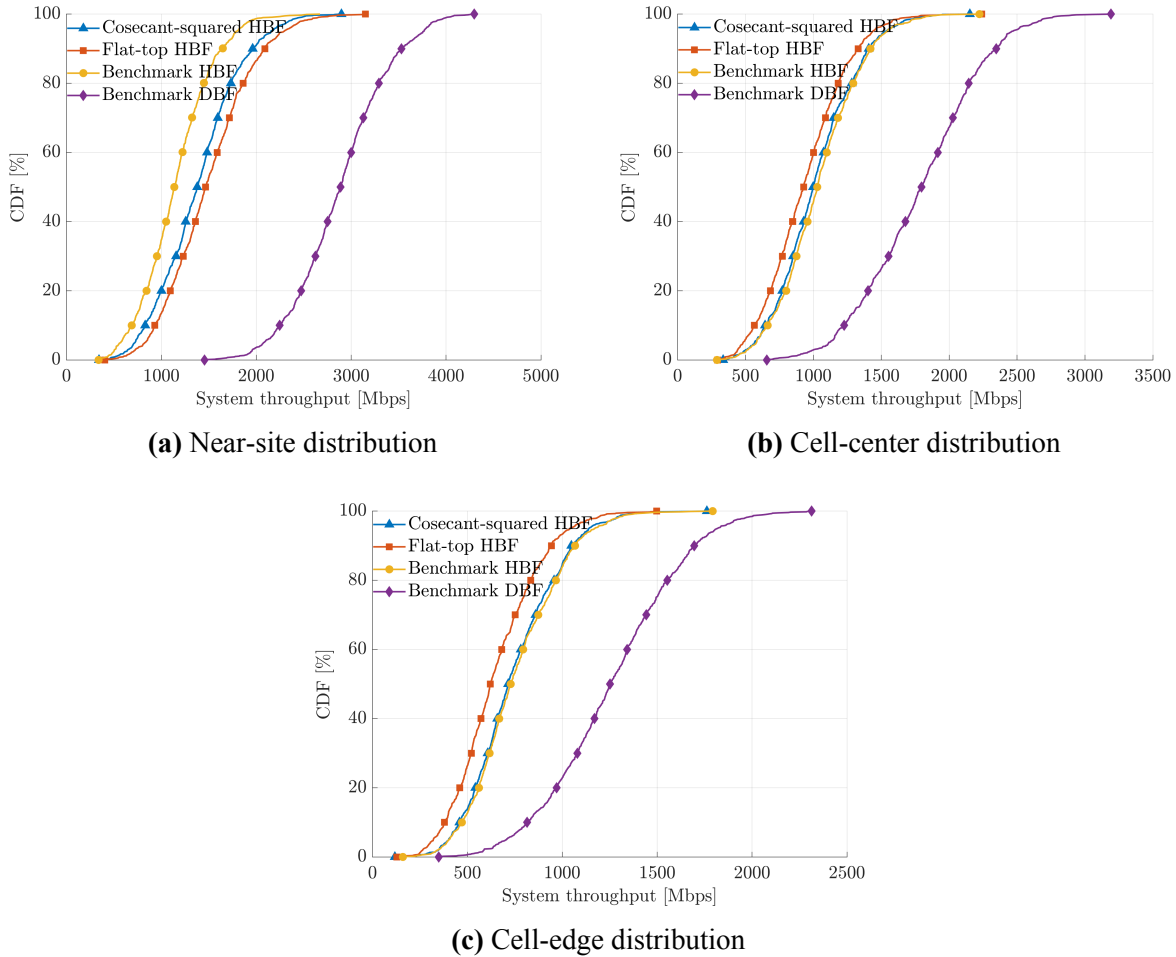
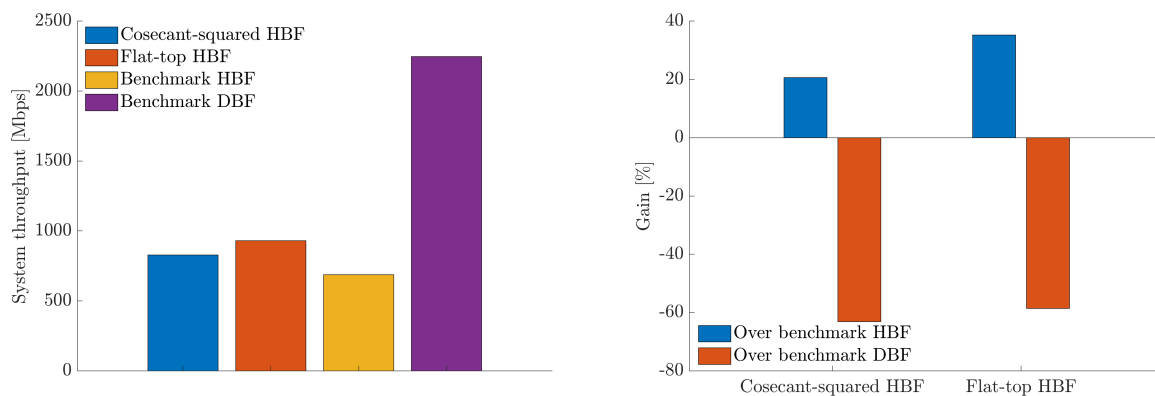
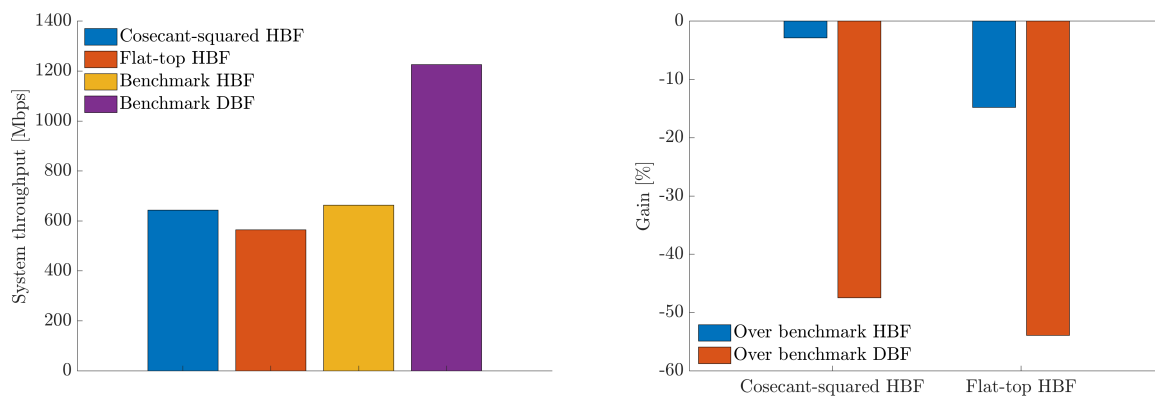


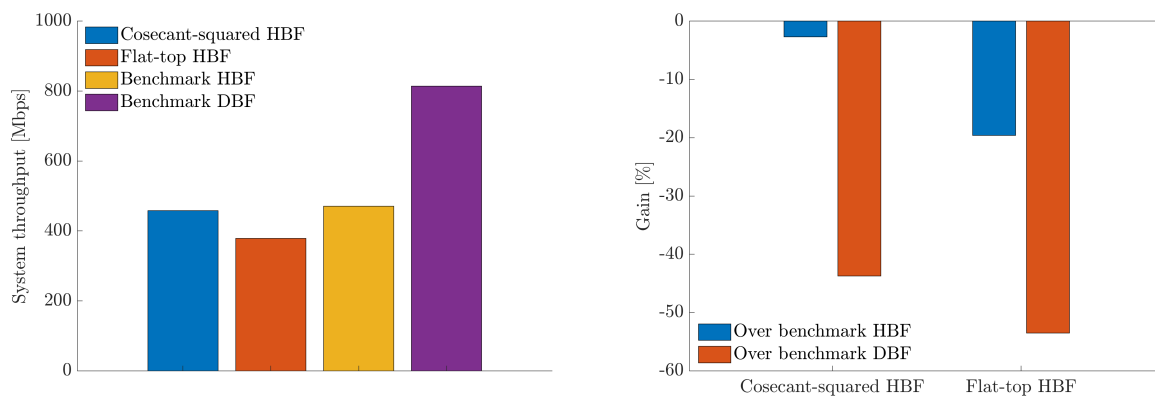
**Figure 4.7:** CDF curves for different beamforming architectures with non-uniformly distributed 10 UEs under the LoS scenario



(a) Near-site distribution



(b) Cell-center distribution



(c) Cell-edge distribution

**Figure 4.8:** Comparison of shaped HBF structures and benchmarks with non-uniformly distributed 10 UEs under the LoS scenario

To investigate the performance variation of shaped HBF structures with mixed user distributions, their gain over the benchmark HBF when the uniform distribution is mixed with near-site user distribution is presented in Figure 4.9. Herein, the mixing ratio varies from 0 to 1 which represents the transformation of pure uniform distribution to pure near-site distribution. The cosecant-squared HBF generally always performs better than the benchmark HBF, and the gain ranges from  $-2\%$  to  $20.6\%$ . For the flat-top HBF, even though it outperforms the cosecant-squared HBF after a mixing ratio of about 0.6, the performance decrement with a low mixing ratio (0 to 0.3) is not negligible.

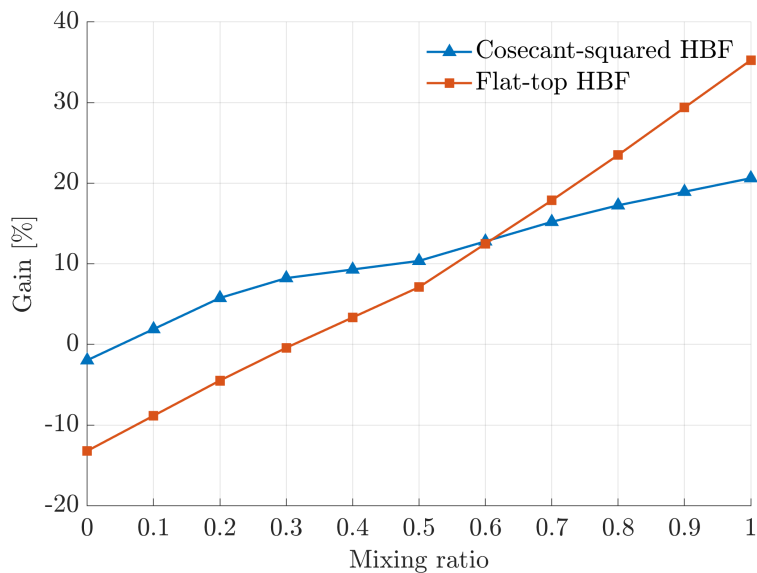


**Figure 4.9:** Comparison of shaped HBF structures and the benchmark HBF with mixed uniform and near-site user distributions under the LoS scenario (10 UEs)

The same studies are repeated for 20 UEs. The comparison of shaped HBF structures and the benchmarks in terms of the 10th percentile system throughput and the gain is plotted in Figure 4.11. When the users are uniformly distributed within the cell, the cosecant-squared HBF again shows a similar performance compared to the benchmark HBF ( $-3.3\%$ ). While the flat-top HBF has a performance degradation of  $14\%$ . In the near-site distribution, the performance increment with the cosecant-squared HBF and flat-top HBF is  $21.8\%$  and  $31.7\%$  respectively. The system gain in both methods is similar in comparison to the 10 UEs case ( $20.6\%$  and  $35.3\%$  for the cosecant-squared HBF and flat-top HBF respectively). For the other two cases of non-uniform distributions, the shaped HBF approaches perform worse than the benchmark HBF, and the performance drop is similar compared to the 10 UEs case.

When there are more UEs in the cell, due to the multiuser diversity effect as explained in Section 4.2, the system performance is improved for all beamforming architectures and user distributions. For example, the 10th percentile system throughput of the benchmark HBF with uniformly distributed users is increased from 1026 Mbps to 1354 Mbps. However, the performance improvement of the DBF approach is more remarkable than the HBF method since it has full beamforming flexibility. This can be observed in Figure 4.11 where the DBF approach has an approximately  $10\%$  additional performance gain compared to the 10 UEs case in Figure 4.6 and 4.8.

Next, the performance variation of shaped HBF structures versus the benchmark HBF with mixed uniform distribution and near-site user distribution is shown in Figure 4.10. The gain variation as a function of the mixing ratio is similar compared to the 10 UEs case in Figure 4.9. The two curves intersect at a mixing ratio of about 0.55. The cosecant-squared HBF again demonstrates a better performance than flat-top HBF since it is more robust against the traffic flow and mobility of the users in such mixed user distributions.

In the above discussion, we have evaluated the system performance of deploying diverse beamforming architectures with uniformly/non-uniformly distributed 10/20 UEs under the LoS scenario. The trade-offs of system performance versus computational/RF hardware complexity between DBF and HBF beamforming methods are demonstrated. When the users are uniformly distributed, the cosecant-squared HBF shows a similar performance compared with the benchmark HBF, and they both outperform the flat-top HBF considerably. Under non-uniform user distributions, shaped HBF structures bring significant performance gain if the users are located near the base station; when the users are distributed further away from the site, the benchmark HBF generally has better performance. If considering mixed user distributions, the cosecant-squared HBF outperforms flat-top HBF and benchmark HBF since it is more robust with respect to differences in spatially heterogeneous traffic distributions. In addition, the interference with drones, airplanes, and high-rise buildings above the horizon (i.e., when  $\theta \leq 0^\circ$  in Figure 3.15) will be potentially much reduced. Safety issues related to vertical compliance distance (i.e., strong harmful radiations near the base station) are avoided as well. In the next section, the system performance with the NLoS scenario will be explored.

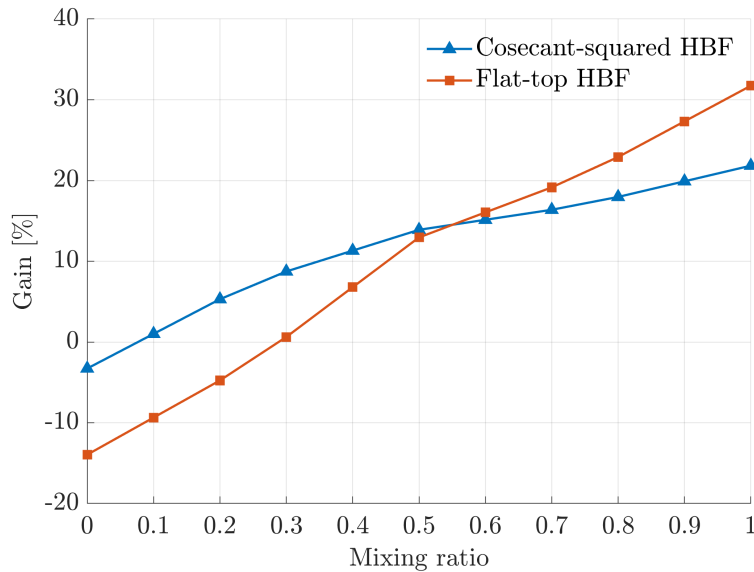
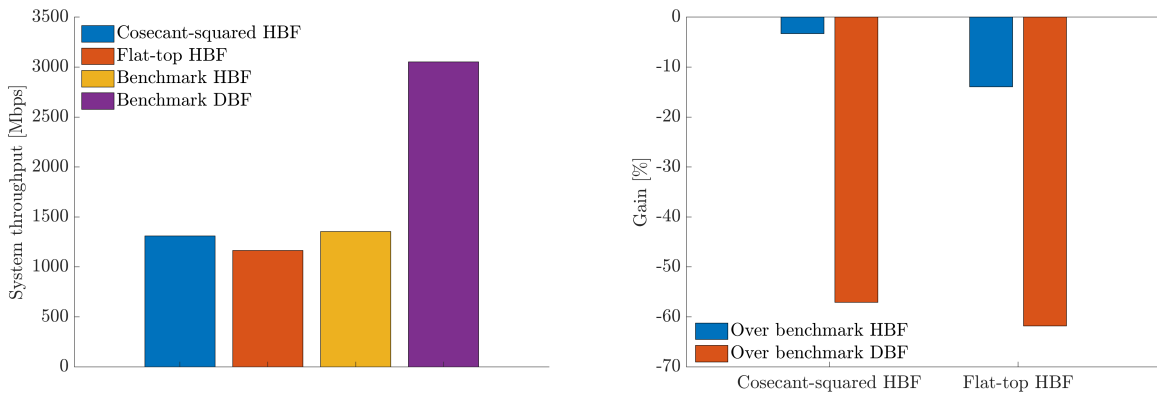
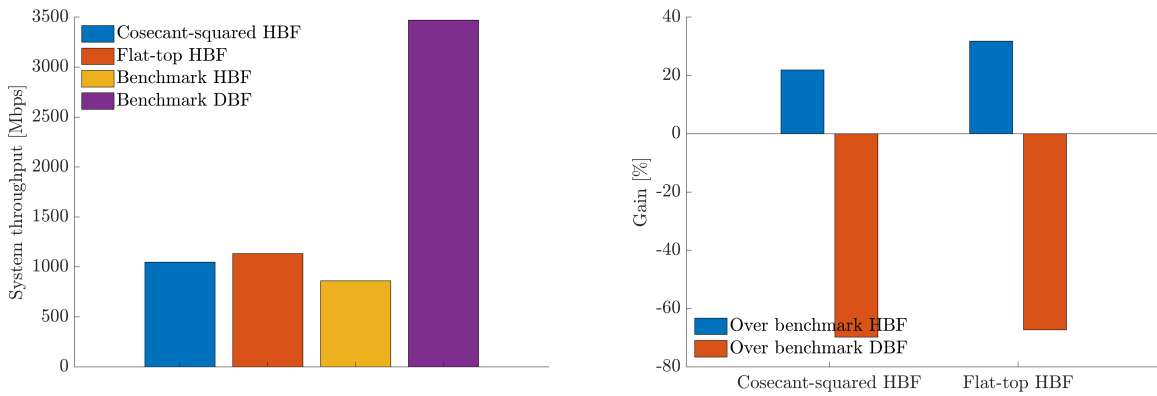


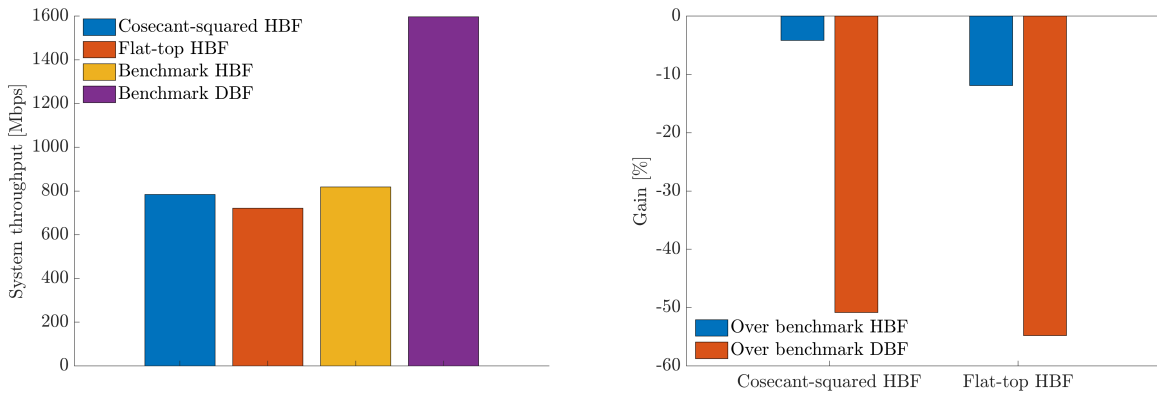
**Figure 4.10:** Comparison of shaped HBF structures and the benchmark HBF with mixed uniform and near-site user distributions under the LoS scenario (20 UEs)



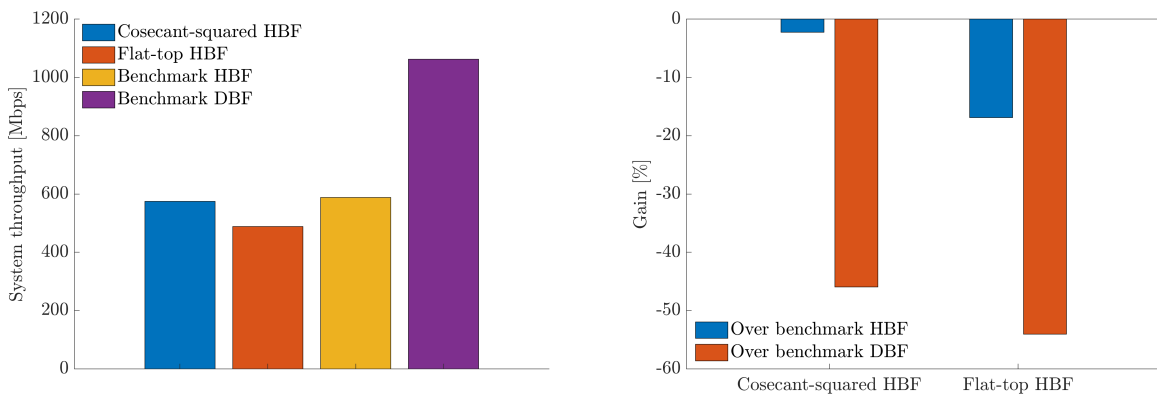
(a) Uniform distribution



(b) Near-site distribution



(c) Cell-center distribution



(d) Cell-edge distribution

**Figure 4.11:** Comparison of shaped HBF structures and benchmarks with uniformly and non-uniformly distributed 20 UEs under the LoS scenario

### 4.3.2. Non-Line-of-Sight Scenario

The simulation results of the NLoS scenario are discussed in this section (see Appendix B for the 10th percentile CDF values). Herein, the number of UEs is set to 10. The CDF curves for various beamforming structures in heterogeneous user distributions are shown in Figure 4.12. Due to severe signal blockage of mm-Waves under the NLoS scenario, the system performance has dropped dramatically compared to the LoS scenario. For example, the 10th percentile system throughput of benchmark DBF in uniform user distribution is decreased from 1924 Mbps to 367 Mbps. However, the DBF approach still has better performance in comparison to HBF methods.

From the uniform to near-site user distribution, there is a performance improvement in terms of the achieved 10th percentile system throughput of 102 Mbps, 143 Mbps, and 109 Mbps for the cosecant-squared HBF, flat-top HBF, and benchmark HBF respectively. This observation differs from the LoS scenario where we see a performance degradation of the cosecant-squared HBF and benchmark HBF. It suggests that under the NLoS scenario, the improvement in channel quality when the users are near the base station dominates over potentially insufficient user separation and a decrement in antenna gain. The benchmark HBF shows an overall better performance than shaped HBF architectures. Particularly, the performance is decreased by 6.3% and 5.6% for the cosecant-squared squared HBF and flat-top HBF respectively compared to the benchmark HBF in the near-site distribution. The results in Figure 4.13b are contrary to the LoS scenario in Figure 4.8a where a significant system performance improvement is observed with shaped HBF structures. It means that the proposed subarray beam pattern shapes do not work well if the direct propagation path of signals is blocked. In QuaDRiGa channel models, the communication environments are modeled with randomness. However, especially with the NLoS scenario, more deterministic environmental information (e.g., the location of the strongest scatterer) is often required to optimally shape the subarray beam pattern. In recent 5G/6G and beyond communication systems, reconfigurable intelligent surfaces (RISs) are proposed as a promising and revolutionized technique for enhancing the spectrum and energy efficiency of wireless systems [42]. These devices are capable of reconfiguring wireless propagation environments by smartly tuning the phase shifts of low-cost reflecting elements. RISs can be installed on large flat surfaces (e.g., buildings and signage) and reflect RF energy around obstacles to create a virtual LoS propagation path between the mm-Wave source and the destination [42]. With such an approach, the impediment of mm-Wave signals blockage can be largely solved. Therefore, the subarray beam pattern of the shaped HBF beamforming structure can be optimized with deterministic environmental information on RIS surfaces to improve its system performance under the NLoS scenario.

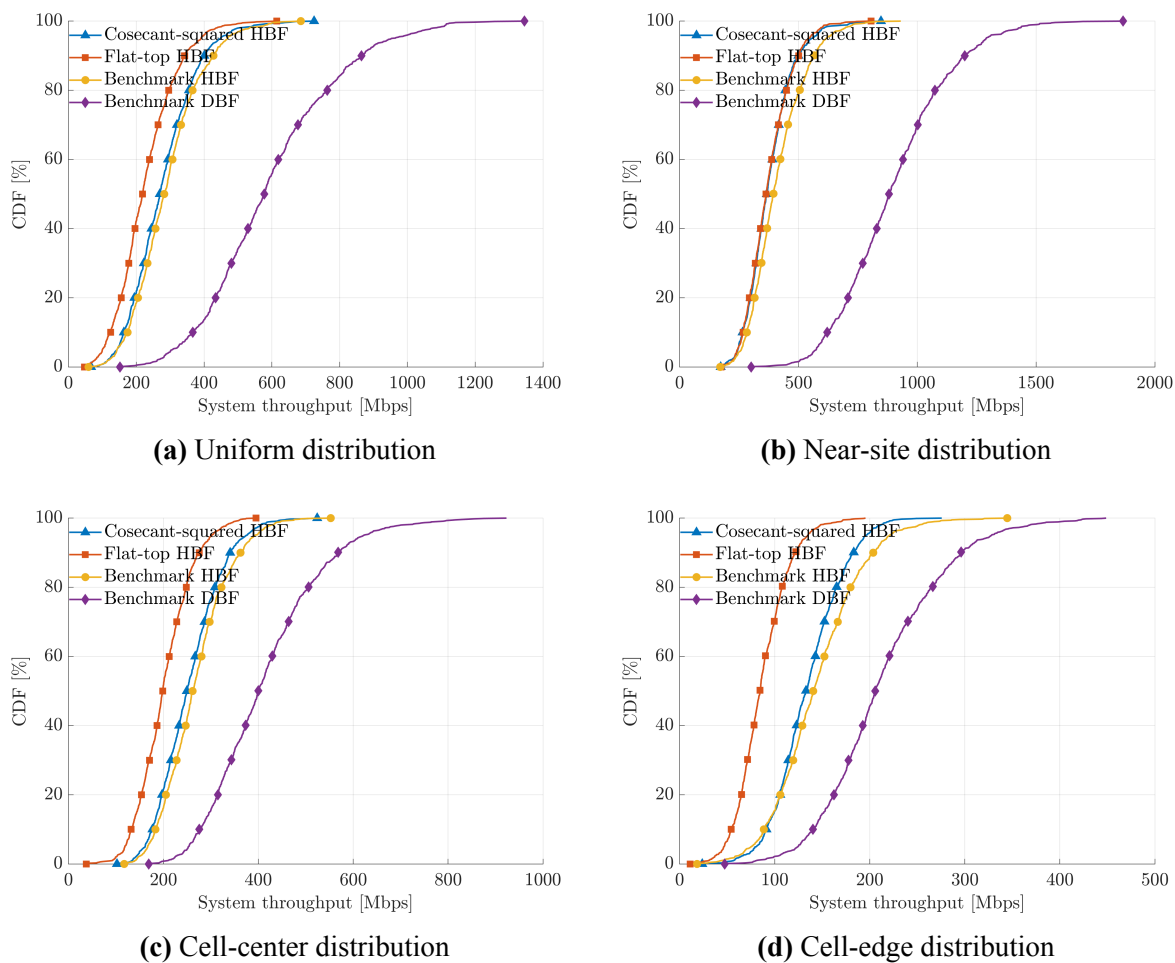
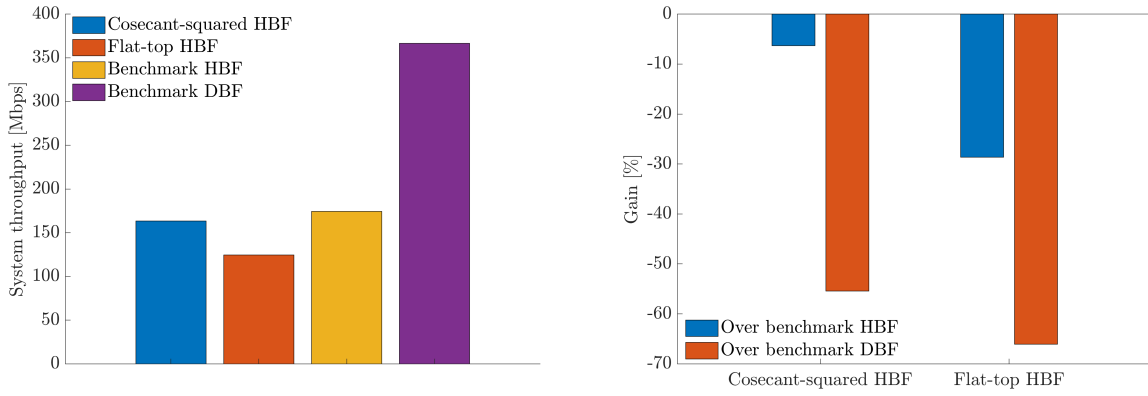
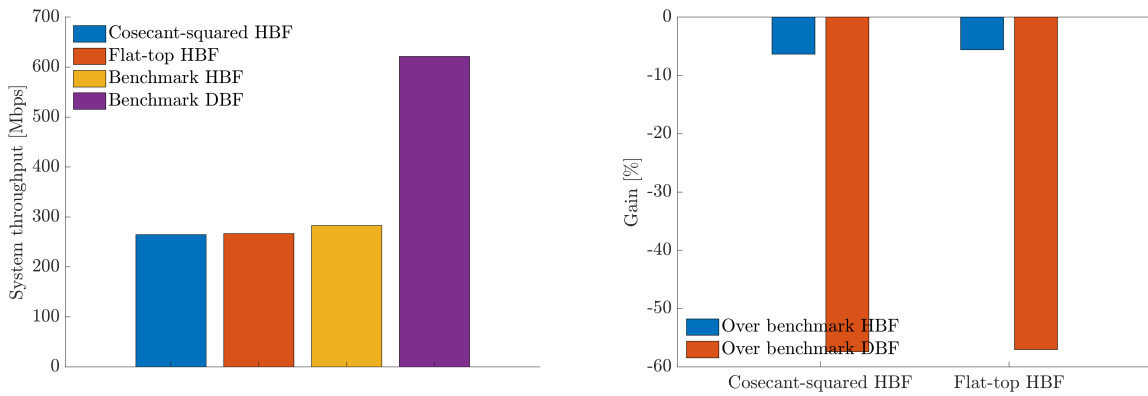


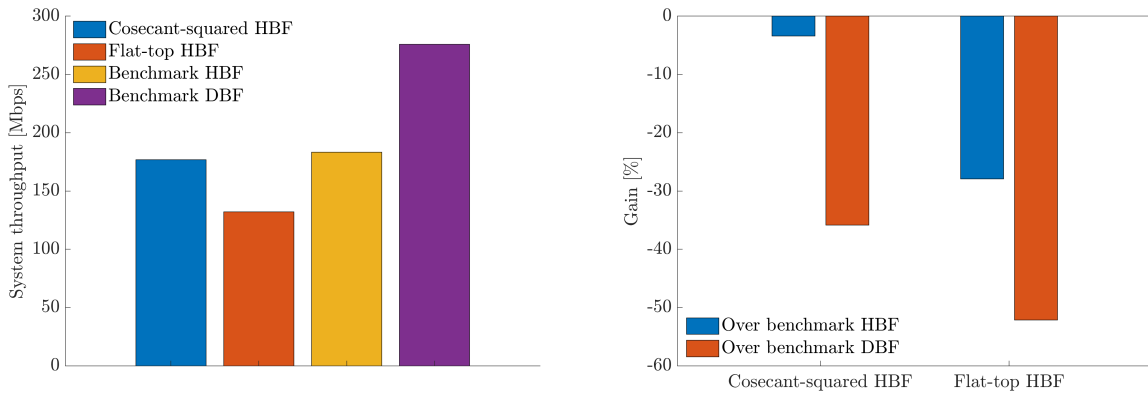
**Figure 4.12:** CDF curves for different beamforming architectures with uniformly and non-uniformly distributed 10 UEs under the NLoS scenario



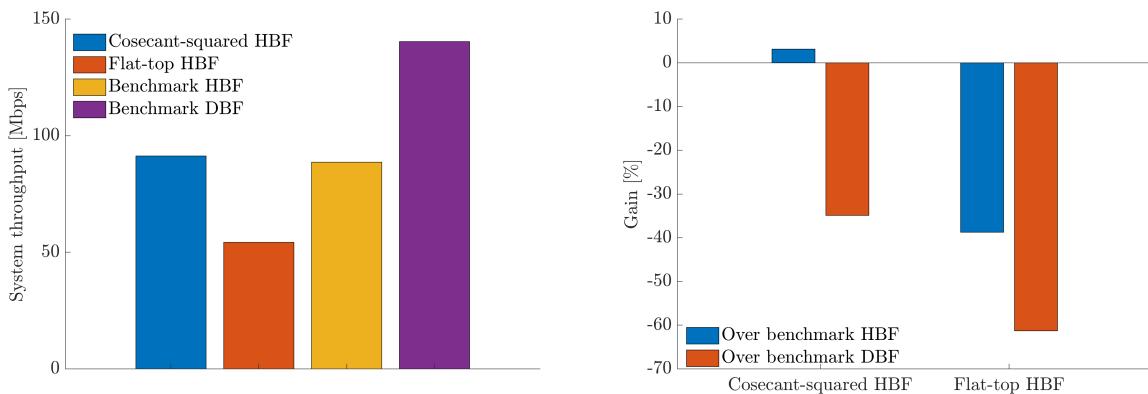
(a) Uniform distribution



(b) Near-site distribution



(c) Cell-center distribution



(d) Cell-edge distribution

**Figure 4.13:** Comparison of shaped HBF structures and benchmarks with uniformly and non-uniformly distributed 10 UEs under the NLoS scenario

# 5

## Conclusion and Recommendations

With its appealing system performance versus computational/hardware complexity trade-offs, the hybrid beamforming (HBF) approach has attracted wide attention in antenna design and wireless communication communities in recent years. A promising HBF technique for mm-Wave massive MIMO 5G base stations is to employ vertically-oriented series-fed subarrays generating a fixed beam pattern in the elevation plane. The current research level in the field of antenna design fails (due to the lack of knowledge on mobile networks) to assess the system performance of such an approach in realistic mm-Wave propagation environments. This creates uncertainty and hesitation for the service providers to invest in such a technique.

**This thesis merges the gap between distinct domains of signal processing, antenna design, and wireless communication by creating a novel cross-disciplinary bridge. The innovative research idea is to identify a suitable (in terms of the 10th percentile system throughput) subarray beam pattern of the HBF structure depending on the user distribution and propagation scenario. To achieve this, a novel 5G NR system-level simulation model is proposed and integrated with antenna array/beamforming architecture designs. It is demonstrated, for the first time, that under mixed uniform and non-uniform user distributions with increased probability for the near-site distribution, the shaped HBF structure with a cosecant-squared beam pattern can provide more than 20% system performance gain.**

In detail, in the thesis framework, we have evaluated the performance of deploying fully digital beamforming (DBF) and hybrid beamforming (HBF) with/without subarray beam pattern shaping in uniform/non-uniform user distributions and LoS/NLoS propagation scenarios at the 26 GHz frequency band using a novel 5G NR system-level simulation model. To contribute to the state-of-the-art approaches, the proposed 5G NR SLS model integrates realistic mm-Wave channel models, the antenna dual-polarization, the link-to-system mapping interface, and two smart radio resource management schemes (i.e., the proportional fairness scheduling and semi-orthogonal user selection). Moreover, the performance of proposed HBF structures with shaped beam patterns is simulated in heterogeneous user distributions considering the traffic flow and mobility of users.

The research questions listed in Section 1.3 are answered here. To answer research question 1, the system performance versus computational/hardware complexity trade-offs of having the DBF and HBF beamforming methods are demonstrated. Specifically, although deploying the DBF architecture with full beamforming flexibility is expensive in the enormous computational resources required and RF front-end structure, it significantly outperforms HBF beamforming methods. Simulation results show that with uniformly distributed 10 UEs under the LoS scenario, the DBF method outperforms the cosecant-squared HBF and flat-top HBF by 47.7% and 53.7%

respectively. When there are 20 UEs in the cell, the DBF approach gives an approximately 10% additional performance gain over shaped HBF methods.

To answer research question 2, the HBF architectures with a cosecant-squared beam pattern, a flat-top beam pattern, and without beam pattern shaping (benchmark) are proposed. They are generated conditioned on the user distributions and cover areas where users are located. Under the LoS scenario, the cosecant-squared HBF performs similarly in the uniform user distribution compared with the benchmark HBF. In the near-site distribution, a system performance improvement of 20.6% is achieved with 10 UEs. The performance gain is similar when there are 20 UEs in the cell. In the cell-center and cell-edge distributions, the cosecant-squared HBF again performs similarly compared to the benchmark HBF. The flat-top HBF is remarkable in serving users near the base station. In that user distribution, a system performance gain of 35.3% and 31.7% is demonstrated in the presence of 10 UEs and 20 UEs respectively. However, the performance degradation with such a beamforming method in the uniform distribution and when users are far away from the site (i.e., the cell-center and cell-edge distributions) is not negligible. Under the NLoS scenario, the shaped HBF approaches do not perform well and the benchmark HBF shows an overall better performance.

In conclusion, the HBF beamforming structure with a cosecant-squared subarray beam pattern presents a promising system performance in uniform and non-uniform user distributions under the LoS scenario. It is more robust against differences in spatially heterogeneous traffics than the flat-top HBF and benchmark HBF. The interference to aircraft and high-rise buildings above the horizon, and strong harmful radiations near the base station will be potentially much reduced by using such a beam pattern shape as well. Due to the sensitivity of mm-Waves to signal blockage and propagation loss, more deterministic environment information and radio channel modeling are required to improve the system performance of the shaped HBF beamforming approach under the NLoS scenario.

The suggested improvements of the thesis work and several promising future research directions are outlined below:

- To further develop the proposed 5G NR SLS model: (i) the rank strategy can be adapted at each TTI. (ii) The CSI feedback delay between the BS and UEs can be added to model imperfect channel state information (I-CSI). (iii) The system performance variations of using different beamforming algorithms (e.g., dirty paper coding (DPC) and vector perturbation (VP)) can be explored.
- To have more realistic antenna models: (i) the mutual coupling effect within subarray radiating elements and among distinct subarrays can be added. (ii) Dual-polarized HBF antennas with subarray beam pattern shaping can be designed in CST Studio Suite. (iii) The beam squint effect can be addressed.
- In the simulation setting, the number of TTIs should be increased (e.g., 1000) to properly apply the PF scheduling algorithm.
- The system performance variations of deploying different beamforming architectures can be evaluated in other propagation environments (e.g., rural, indoor office).
- The deployed network layout with a single site can be expanded to multiple BSs to include intersite interference. Based on that, the performance potential of distributed MIMO (D-MIMO) combined with MU-MIMO with the shaped HBF beamforming approach can be assessed.

- The signal blockage issue of mm-Waves under the NLoS scenario can be largely solved with RIS surfaces. This implies more deterministic modeling of the communication environments (e.g., using ray tracing in FEKO [43]). The subarray beam pattern shape of the HBF antenna can be optimized based on known information about RIS surfaces to improve the system performance.

# References

- [1] W. Hong, Z. H. Jiang, C. Yu, J. Zhou, P. Chen, Z. Yu, H. Zhang, B. Yang, X. Pang, M. Jiang, Y. Cheng, M. K. T. Al-Nuaimi, Y. Zhang, J. Chen, and S. He, “Multibeam Antenna Technologies for 5G Wireless Communications,” *IEEE Transactions on Antennas and Propagation*, vol. 65, no. 12, pp. 6231–6249, 2017. DOI: 10.1109/TAP.2017.2712819.
- [2] H. Q. Ngo, E. G. Larsson, and T. L. Marzetta, “Energy and Spectral Efficiency of Very Large Multiuser MIMO Systems,” *IEEE Transactions on Communications*, vol. 61, no. 4, pp. 1436–1449, 2013. DOI: 10.1109/TCOMM.2013.020413.110848.
- [3] E. Bobrov, B. Chinyaev, V. Kuznetsov, H. Lu, D. Minenkov, S. Troshin, D. Yudakov, and D. Zaev, “Adaptive Regularized Zero-Forcing Beamforming in Massive MIMO with Multi-Antenna Users,” 2022. DOI: 10.21203/rs.3.rs-1780852/v1.
- [4] S. Chen and J. Zhao, “The Requirements, Challenges, and Technologies for 5G of Terrestrial Mobile Telecommunication,” *IEEE Communications Magazine*, vol. 52, no. 5, pp. 36–43, 2014. DOI: 10.1109/MCOM.2014.6815891.
- [5] M. V. Patil, S. Pawar, and Z. Saquib, “Coding Techniques for 5G Networks: A Review,” in *2020 3rd International Conference on Communication System, Computing and IT Applications (CSCITA)*, 2020, pp. 208–213. DOI: 10.1109/CSCITA47329.2020.9137797.
- [6] U. Mutlu and Y. Kabalcı, “Performance Analyses of Hybrid-ARQ in Fifth Generation New Radio,” in *2021 3rd Global Power, Energy and Communication Conference (GPECOM)*, 2021, pp. 269–274. DOI: 10.1109/GPECOM52585.2021.9587674.
- [7] S. Nagul, “A Review on 5G Modulation Schemes and Their Comparisons for Future Wireless Communications,” in *2018 Conference on Signal Processing And Communication Engineering Systems (SPACES)*, 2018, pp. 72–76. DOI: 10.1109/SPACES.2018.8316319.
- [8] D. M. Pozar, *Microwave Engineering*, 3rd ed. Hoboken, NJ: John Wiley & Sons, 2005.
- [9] I. Ahmed, H. Khammari, A. Shahid, A. Musa, K. S. Kim, E. De Poorter, and I. Moerman, “A Survey on Hybrid Beamforming Techniques in 5G: Architecture and System Model Perspectives,” *IEEE Communications Surveys & Tutorials*, vol. 20, no. 4, pp. 3060–3097, 2018. DOI: 10.1109/COMST.2018.2843719.
- [10] T. L. Marzetta, “Noncooperative Cellular Wireless with Unlimited Numbers of Base Station Antennas,” *IEEE Transactions on Wireless Communications*, vol. 9, no. 11, pp. 3590–3600, 2010. DOI: 10.1109/TWC.2010.092810.091092.
- [11] A. Roederer, J. Puskely, Y. Aslan, and A. Yarovoy, “Shaped Elevation Patterns for 5G Base Stations,” in *2021 IEEE International Symposium on Antennas and Propagation and USNC-URSI Radio Science Meeting (APS/URSI)*, 2021, pp. 795–796. DOI: 10.1109/APS/URSI47566.2021.9704580.
- [12] T. Mikulasek, J. Puskely, A. G. Yarovoy, J. Lacik, and H. Arthaber, “Transverse Slot With Control of Amplitude and Phase for Travelling-Wave SIW Antenna Arrays,” *IET*

- Microwaves, Antennas & Propagation*, vol. 14, no. 15, pp. 1943–1946, 2020. DOI: 10.1049/iet-map.2020.0069.
- [13] J. Puskely, T. Mikulasek, Y. Aslan, A. Roederer, and A. Yarovoy, “5G SIW-Based Phased Antenna Array With Cosecant-Squared Shaped Pattern,” *IEEE Transactions on Antennas and Propagation*, vol. 70, no. 1, pp. 250–259, 2022. DOI: 10.1109/TAP.2021.3098577.
- [14] T. Kopacz and D. Heberling, “Impact of the Elevation Scanning Angle on the Vertical Compliance Distance of 5G Massive MIMO Antennas,” in *2019 13th European Conference on Antennas and Propagation (EuCAP)*, 2019, pp. 1–5.
- [15] S. Salman, Y. Aslan, J. Puskely, A. Roederer, and A. Yarovoy, “System Modeling and Simulation in 5G: A Hybrid Beamforming Approach With Power Flux Equalization in the Elevation Plane,” *2019 49th European Microwave Conference (EuMC)*, 2019. DOI: 10.23919/eumc.2019.8910782.
- [16] T. Kuehne, X. Song, G. Caire, K. Rasilainen, T. H. Le, M. Rossi, I. Ndip, and C. Fager, “Performance Simulation of a 5G Hybrid Beamforming Millimeter-Wave System,” in *WSA 2020; 24th International ITG Workshop on Smart Antennas*, 2020, pp. 1–6.
- [17] *QuaDRiGa: The Next Generation Radio Channel Model*. [Online]. Available: <https://quadriga-channel-model.de/>.
- [18] *CST Studio Suite: Electromagnetic Field Simulation Software*. [Online]. Available: <https://www.3ds.com/products-services/simulia/products/cst-studio-suite/>.
- [19] S. Jaeckel, L. Raschkowski, K. Börner, L. Thiele, F. Burkhardt, and E. Eberlein, “QuaDRiGa - Quasi Deterministic Radio Channel Generator, User Manual and Documentation,” Fraunhofer Heinrich Hertz Institute, Tech. Rep., version 2.6.1, 2021.
- [20] N. H. Mahmood, G. Berardinelli, F. M. L. Tavares, M. Lauridsen, P. Mogensen, and K. Pajukoski, “An Efficient Rank Adaptation Algorithm for Cellular MIMO Systems With IRC Receivers,” in *2014 IEEE 79th Vehicular Technology Conference (VTC Spring)*, 2014, pp. 1–5. DOI: 10.1109/VTCSpring.2014.7022820.
- [21] X. Song, T. Kühne, and G. Caire, “Fully-/Partially-Connected Hybrid Beamforming Architectures for mmWave MU-MIMO,” *IEEE Transactions on Wireless Communications*, vol. 19, no. 3, pp. 1754–1769, 2020. DOI: 10.1109/TWC.2019.2957227.
- [22] S. Wan, H. Zhu, K. Kang, and H. Qian, “On the Performance of Fully-Connected and Sub-Connected Hybrid Beamforming System,” *IEEE Transactions on Vehicular Technology*, vol. 70, no. 10, pp. 11 078–11 082, 2021. DOI: 10.1109/TVT.2021.3109300.
- [23] J. Yang, H. Zhao, W. Wang, and C. Zhang, “An Effective SINR Mapping Models for 256QAM in LTE-Advanced System,” in *2014 IEEE 25th Annual International Symposium on Personal, Indoor, and Mobile Radio Communication (PIMRC)*, 2014, pp. 343–347. DOI: 10.1109/PIMRC.2014.7136187.
- [24] K. Sayana, J. Zhuang, and K. A. Stewart, “Link Performance Abstraction Based on Mean Mutual Information per Bit (MMIB) of the LLR Channel,” 2007.
- [25] Y. Barayan and I. Kostanic, “Performance Evaluation of Proportional Fairness Scheduling in LTE,” in *Proceedings of the World Congress on Engineering and Computer Science*, vol. 2, 2013, pp. 712–717.

- [26] A. M. Nor, O. Fratu, S. Halunga, A. Alyosef, Z. D. Zaharis, S. Rizou, and P. I. Lazaridis, "Demand Based Proportional Fairness Scheduling for 5G eMBB Services," in *2022 IEEE International Black Sea Conference on Communications and Networking (BlackSeaCom)*, 2022, pp. 263–268. DOI: 10.1109/BlackSeaCom54372.2022.9858321.
- [27] T. Yoo and A. Goldsmith, "On the Optimality of Multiantenna Broadcast Scheduling Using Zero-Forcing Beamforming," *IEEE Journal on Selected Areas in Communications*, vol. 24, no. 3, pp. 528–541, 2006. DOI: 10.1109/JSAC.2005.862421.
- [28] S. Braam, R. Litjens, P. Smulders, and W. IJntema, "Assessment of Distributed Multi-user MIMO Transmission in 5G Networks," *Proceedings of the 18th ACM Symposium on Mobility Management and Wireless Access*, 2020. DOI: 10.1145/3416012.3424629.
- [29] 3GPP TR 36.873 v12.5.0, "Study on 3D Channel Model for LTE," Tech. Rep., 2017.
- [30] 3GPP TR 38.901 v16.1.0, "Study on Channel Model for Frequencies from 0.5 to 100 GHz," Tech. Rep., 2019.
- [31] G. Lebrun, T. Ying, and M. Faulkner, "MIMO Transmission Over a Time-Varying Channel Using SVD," in *Global Telecommunications Conference, 2002. GLOBECOM '02. IEEE*, vol. 1, 2002, 414–418 vol.1. DOI: 10.1109/GLOCOM.2002.1188112.
- [32] L. Sun and M. R. McKay, "Eigen-Based Transceivers for the MIMO Broadcast Channel With Semi-Orthogonal User Selection," *IEEE Transactions on Signal Processing*, vol. 58, no. 10, pp. 5246–5261, 2010. DOI: 10.1109/TSP.2010.2053709.
- [33] E. Bobrov, D. Kropotov, S. Troshin, and D. Zaev, "Study on Precoding Optimization Algorithms in Massive MIMO System With Multi-Antenna Users," *Optimization Methods and Software*, pp. 1–16, 2022. DOI: 10.1080/1055642788.2022.2091564.
- [34] B. Ren, Y. Wang, S. Sun, Y. Zhang, X. Dai, and K. Niu, "Low-Complexity MMSE-IRC Algorithm for Uplink Massive MIMO Systems," *Electronics Letters*, vol. 53, no. 14, pp. 972–974, 2017. DOI: 10.1049/e1.2017.1133.
- [35] S. Lagen, K. Wanuga, H. Elkotby, S. Goyal, N. Patriciello, and L. Giupponi, "New Radio Physical Layer Abstraction for System-Level Simulations of 5G Networks," in *ICC 2020 - 2020 IEEE International Conference on Communications (ICC)*, 2020, pp. 1–7. DOI: 10.1109/ICC40277.2020.9149444.
- [36] Z. Hanzaz and H. D. Schotten, "Analysis of Effective SINR Mapping Models for MIMO OFDM in LTE System," in *2013 9th International Wireless Communications and Mobile Computing Conference (IWCMC)*, 2013, pp. 1509–1515. DOI: 10.1109/IWCMC.2013.6583780.
- [37] E. Tuomaala and H. Wang, "Effective SINR Approach of Link to System Mapping in OFDM/Multi-carrier Mobile Network," in *2005 2nd Asia Pacific Conference on Mobile Technology, Applications and Systems*, 2005, 5 pp.–5. DOI: 10.1109/MTAS.2005.243791.
- [38] I. Kim, J. Um, and S. Park, "Implementation and Performance Evaluation of 256-QAM in Vienna System Level Simulator," in *2018 20th International Conference on Advanced Communication Technology (ICACT)*, 2018, pp. 556–559. DOI: 10.23919/ICACT.2018.8323830.

- 
- [39] 3GPP TS 36.213 v14.2.0, “Evolved Universal Terrestrial Radio Access (E-UTRA), Physical Layer Procedures,” Tech. Spec., 2017.
- [40] R. Sandanalakshmi, S. Mumtaz, and K. Saidul, “Enhanced Algorithm for MIESM,” *Recent Patents on Signal Processing*, vol. 1, pp. 1–7, 2009.
- [41] J. Puskely, Y. Aslan, A. Roederer, and A. Yarovoy, “SIW Based Antenna Array With Power Equalization in Elevation Plane for 5G Base Stations,” in *12th European Conference on Antennas and Propagation (EuCAP 2018)*, 2018, pp. 1–5. DOI: 10.1049/cp.2018.0424.
- [42] C. Pan, H. Ren, K. Wang, J. F. Kolb, M. ElKashlan, M. Chen, M. Di Renzo, Y. Hao, J. Wang, A. L. Swindlehurst, X. You, and L. Hanzo, “Reconfigurable Intelligent Surfaces for 6G Systems: Principles, Applications, and Research Directions,” *IEEE Communications Magazine*, vol. 59, no. 6, pp. 14–20, 2021. DOI: 10.1109/MCOM.001.2001076.
- [43] *FEKO: Solving Connectivity, Compatibility, and Radar Challenges*. [Online]. Available: <https://altair.com/feko>.

# A

## Simulation Results for the Line-of-Sight Scenario

The CDF curves (only the 20 UEs case) and 10th percentile CDF values for various beamforming architectures in heterogeneous user distributions with 10 UEs and 20 UEs under the LoS scenario can be found below.

| Beamforming architectures       | 10th percentile system throughput [Mbps] |
|---------------------------------|--|
| <b>Uniform distribution</b>     |  |
| Cosecant-squared HBF            | 1006                                     |
| Flat-top HBF                    | 890                                      |
| Benchmark HBF                   | 1026                                     |
| Benchmark DBF                   | 1924                                     |
| <b>Near-site distribution</b>   |  |
| Cosecant-squared HBF            | 829                                      |
| Flat-top HBF                    | 930                                      |
| Benchmark HBF                   | 687                                      |
| Benchmark DBF                   | 2247                                     |
| <b>Cell-center distribution</b> |  |
| Cosecant-squared HBF            | 644                                      |
| Flat-top HBF                    | 565                                      |
| Benchmark HBF                   | 663                                      |
| Benchmark DBF                   | 1226                                     |
| <b>Cell-edge distribution</b>   |  |
| Cosecant-squared HBF            | 458                                      |
| Flat-top HBF                    | 379                                      |
| Benchmark HBF                   | 471                                      |
| Benchmark DBF                   | 814                                      |

**Table A.1:** 10th percentile CDF values for different beamforming architectures with uniformly and non-uniformly distributed 10 UEs under the LoS scenario

| Beamforming architectures       | 10th percentile system throughput [Mbps] |
|---------------------------------|--|
| <b>Uniform distribution</b>     |  |
| Cosecant-squared HBF            | 1310                                     |
| Flat-top HBF                    | 1165                                     |
| Benchmark HBF                   | 1354                                     |
| Benchmark DBF                   | 3053                                     |
| <b>Near-site distribution</b>   |  |
| Cosecant-squared HBF            | 1048                                     |
| Flat-top HBF                    | 1133                                     |
| Benchmark HBF                   | 860                                      |
| Benchmark DBF                   | 3469                                     |
| <b>Cell-center distribution</b> |  |
| Cosecant-squared HBF            | 784                                      |
| Flat-top HBF                    | 721                                      |
| Benchmark HBF                   | 819                                      |
| Benchmark DBF                   | 1596                                     |
| <b>Cell-edge distribution</b>   |  |
| Cosecant-squared HBF            | 574                                      |
| Flat-top HBF                    | 488                                      |
| Benchmark HBF                   | 588                                      |
| Benchmark DBF                   | 1063                                     |

**Table A.2:** 10th percentile CDF values for different beamforming architectures with uniformly and non-uniformly distributed 20 UEs under the LoS scenario

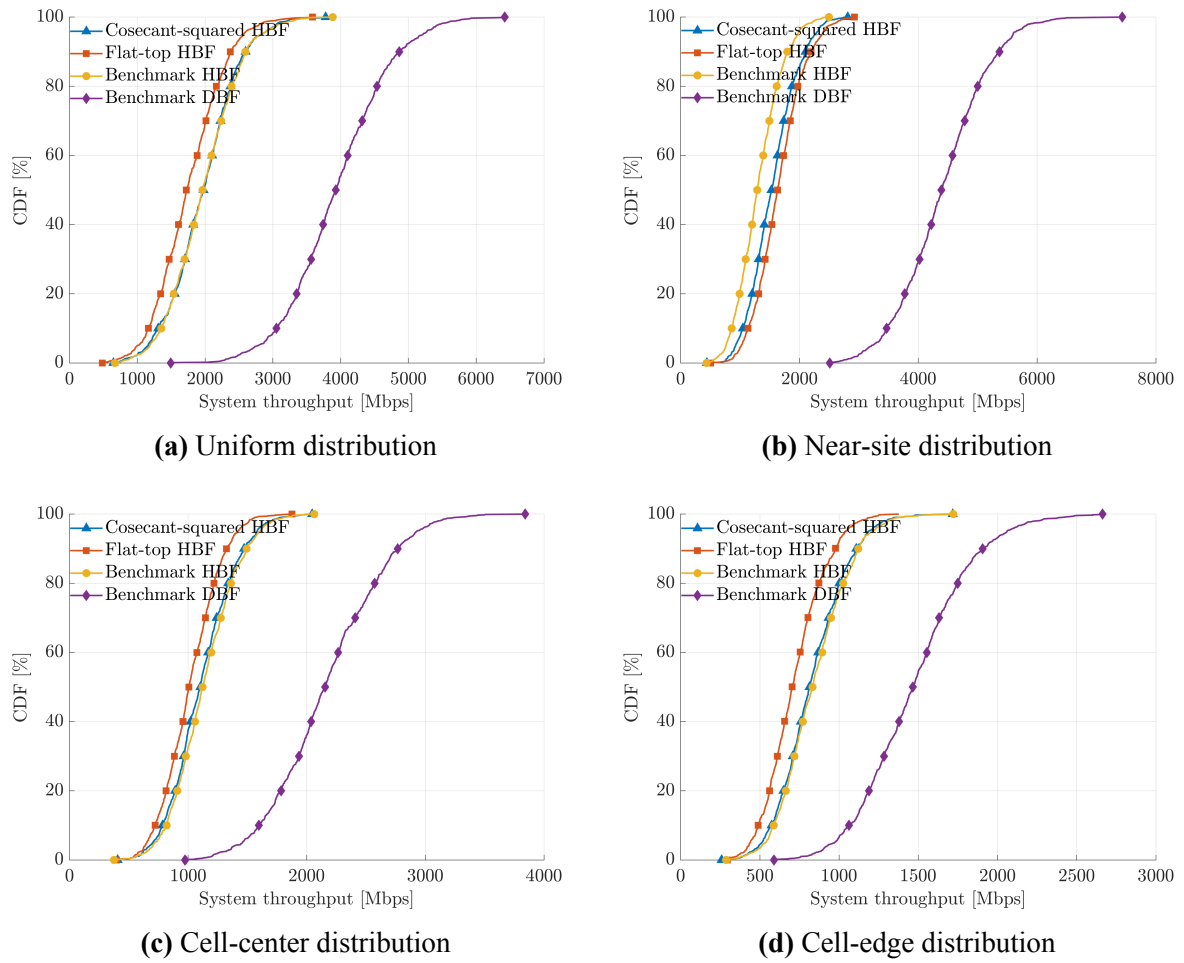


**Figure A.1:** CDF curves for different beamforming architectures with uniformly and non-uniformly distributed 20 UEs under the LoS scenario

# B

## Simulation Results for the Non-Line-of-Sight Scenario

The 10th percentile CDF values for various beamforming architectures in heterogeneous user distributions with 10 UEs under the NLoS scenario are presented in the following table.

| Beamforming architectures       | 10th percentile system throughput [Mbps] |
|---------------------------------|--|
| <b>Uniform distribution</b>     |  |
| Cosecant-squared HBF            | 163                                      |
| Flat-top HBF                    | 124                                      |
| Benchmark HBF                   | 174                                      |
| Benchmark DBF                   | 367                                      |
| <b>Near-site distribution</b>   |  |
| Cosecant-squared HBF            | 265                                      |
| Flat-top HBF                    | 267                                      |
| Benchmark HBF                   | 283                                      |
| Benchmark DBF                   | 621                                      |
| <b>Cell-center distribution</b> |  |
| Cosecant-squared HBF            | 177                                      |
| Flat-top HBF                    | 132                                      |
| Benchmark HBF                   | 183                                      |
| Benchmark DBF                   | 276                                      |
| <b>Cell-edge distribution</b>   |  |
| Cosecant-squared HBF            | 91                                       |
| Flat-top HBF                    | 54                                       |
| Benchmark HBF                   | 89                                       |
| Benchmark DBF                   | 140                                      |

**Table B.1:** 10th percentile CDF values for different beamforming architectures with uniformly and non-uniformly distributed 10 UEs under the NLoS scenario